

Contents lists available at ScienceDirect

Theoretical and Applied Fracture Mechanics

journal homepage: www.elsevier.com/locate/tafmec



Mixed-mode fracture: Combination of Arcan fixture and stereo-DIC

Abdalrhaman Koko a,b,*, Thorsten H. Becker c

- ^a Department of Materials, University of Oxford, Oxford OX1 3PH, United Kingdom
- ^b National Physical Laboratory, Hampton Road, Teddington TW11 OLW, United Kingdom
- ^c Centre for Materials Engineering, Department of Mechanical Engineering, University of Cape Town, Cape Town, South Africa

ARTICLE INFO

Keywords: Arcan fixture J-integral Crack growth Stereo DIC Stress intensity factor

ABSTRACT

To characterise mixed-mode fracture, including mode III, a combination of Arcan fixture, that offers both inplane and out-of-plane loading, and stereo digital image correlation (DIC) has proven valuable for measuring in-plane and out-of-plane surface displacement and deformation fields while allowing for direct stress intensity factor (SIF) extraction throughout the tests, but it comes with many caveats. Using stereo DIC, the mixed mode fracture behaviour of PMMA is analysed using a novel mode decomposition technique that combines experimental and analytical approaches. This technique divides the measured displacement field from digital image correlation into three distinct components: a symmetric field (u^{II}), an in-plane anti-symmetric field (u^{II}), and an out-of-plane antisymmetric field (u^{III}), decomposed by a difference operation on the reflected and non-reflected fields about the crack plane. Then, the strain energy release rate of the crack is calculated for each loading mode using finite elements without knowledge of the sample geometry or nominal loading condition. Our work revealed parasitic loading modes induced by the Archan fixture plus other intrinsic sources related to load accommodation. Nevertheless, the calculated SIFs measured during stable crack growth were normalised using different fracture toughness (K_{IC}) values with K_{IC} of 1.82 \pm 0.32 MPa m^{0.5}, providing the best fit to the fracture loci with an R² of 0.95. This value agrees well with the ASTM-obtained value of 1.7 MPa m^{0.5}.

1. Introduction

Materials and structural engineering may require considering mixed-mode fracture to improve our understanding of complex failure mechanisms. One way to study mixed-mode fracture involves employing an Arcan fixture in tandem with digital image correlation (DIC) to allow for more in-depth investigations into mechanisms that describe fracture under different crack-loading conditions while observing near-crack tip deformations [1–3].

The Arcan fixture is designed to control and vary loading modes across a broad spectrum, from pure mode I to mode II and mode III, as well as mixed-mode conditions, making it particularly suitable for complex fracture scenarios where multiple modes of loading occur simultaneously [4]. It also offers the ability to describe and evaluate fracture using fracture mechanics parameters such as mixed-mode stress intensity factors (SIFs) [4,5]. Meanwhile, DIC provides high-resolution deformation measurements, enabling the observation of localised strain fields at the crack tip and revealing crack propagation patterns. This combination allows measurement of strain evolution near the crack

tip, a crucial aspect in understanding crack behaviour and SIFs. Analysis of DIC data in conjunction with mode-specific loading conditions has been shown to provide valuable information on crack initiation, propagation, and interaction under mixed-mode loading conditions [5–7].

Previous studies have applied the Arcan fixture in combination with DIC to a variety of materials, including steel plates repaired with carbon fibre-reinforced plastic (CFRP) [8,9], off-axis laminated composites [10], and Cold In-place Recycling (CIR) mixtures [4,11,12]. Researchers have observed good consistency between experimental results and modelling predictions by monitoring the fracture process using DIC and calculating SIFs from finite element modelling or analytical solutions [4,12,13]. These studies have shown that the combination of DIC and the Arcan fixture can yield valuable insights into materials' mixed-mode fracture behaviour and has simultaneously facilitated the verification and accuracy assessment of experimental setups [4].

The measured displacement field has typically not been used directly; however, various attempts have been made to extract SIFs from DIC data. McNeill *et al.* [14] in 1987 estimated SIFs by fitting the William's solution to the DIC-measured displacement data ahead of the

^{*} Corresponding author at: Department of Materials, University of Oxford, Oxford OX1 3PH, United Kingdom. *E-mail address*: Abdo.koko@npl.co.uk (A. Koko).

crack tip using a least-squares approach and noted the results' sensitivity (up to 7% [15]) to the accuracy in defining the crack tip location. Later work by Yoneyama et~al.~[16,17] expanded the work for mixed-mode SIFs and higher-order terms. The effects of anisotropy on SIFs were studied [18,19] in single-crystal materials, and the inclusion of T-stress and higher-order terms were shown to improve the accuracy of the regression [20]. Instead of a two-step process, direct approaches have also been proposed, known as integrated~approaches (or IDIC), such as those presented by Roux and Hild [15]. IDIC uses prior information, such as the constituent laws and the applied boundary conditions, to allow for the direct identification of the relevant material parameters of the model.

Poor performance in extracting SIFs from DIC data is often attributed to the uncertainty in measuring the displacement vectors near discontinuities (i.e., near the crack) or edges. However, measurements in the vicinity of the crack tip are typically excluded (e.g., by masking), excluding the steepest displacement gradients. To avoid these issues and obtain an experiment-representative clean displacement field, the use of the Finite Element Method (FEM) for post-processing of the DIC data (hybrid method [21]) has also been explored with in-plane displacement [22].

The strain energy release rate (i.e., J-integral) is a well-established technique often used in the finite element (FE) method for both inplane (2D) or volumetric (3D) analysis. It allows for rather complex crack configurations using the boundary condition of the displacement field or applied loads [23–25]. The J_1 -integral is highly important in modern fracture mechanics, is easy to implement in finite element software, and has been coupled with residual stress, internal tractions, and thermal and electrochemical processes [26]. The existing analytical solutions used to measure standardised fracture toughness are approximated, or can be derived, from the J-integral [27]. The local full displacement field can also extract the strain energy release rate and autonomously monitor crack growth [24]. However, analysing energy release rates using integrals cannot distinguish between mechanical loading conditions (i.e., tensile or compressive mode I, in-plane shear mode II, and out-of-plane shear mode III), which can affect the fracture rate and direction [2]. These local conditions are valuable when the external conditions (e.g., the boundary conditions) are unknown or uncertain. This is especially important on a microscale as knowledge of the mechanical conditions at the crack provides alternatives to the existing methods and analytical solutions that use unreliable micropillars, microcantilevers, and indentation techniques [28,29].

Becker *et al.* [30] first used a full field displacement obtained using DIC to calculate the J-integral using an FE framework with a crack lying on the x_1 axis. They noted that J-integral evaluation requires high-quality displacement field data for the integral to converge and should only consider mode I loading. Breitbarth *et al.* [31] included mode I and II. Further development of the method was carried out by Barhli *et al.* [32], who showed that it was possible to calculate the J-integral using strain field data acquired using energy dispersive X-ray diffraction (EDXD). This opened the possibility of using the HR-EBSD elastic displacement gradient tensors to calculate the J-integral [33,34]. 1

Stren *et al.* [35] proposed an interaction integral (M-integral) approach, and Ishikawa [36] proposed a kinematic decomposition method to separate the loading modes without having to assume an elastic fracture (i.e., J^{I-III} , where I, II and III represents the J specific mode) requiring, however, the exact knowledge of the crack tip. Molteno and Becker [7] introduced the decomposition of the J-integral to facilitate its mode decomposition, only requiring knowledge of the crack plane. Cinar *et al.* [37] introduced an autonomous, more precise, and reliable crack detection algorithm based on the phase congruency method. By applying a refined FE mesh for imported displacement data

around the detected crack and using the commercial ABAQUS software's native capability to separate the different loading modes for 2D and 3D displacement data, it is possible to separate the J-integral in mixed-mode loading conditions [24,25,38].

These methods have yet to be implemented with Arcan testing to illustrate the capability of extracting mixed-mode SIFs from DIC computed displacement data. The premise is that the combination of mixed-mode loading testing using the Arcan geometry and mixed-mode SIF extraction from DIC computed displacement data should provide a more comprehensive understanding of the mechanisms that describe fracture under different crack loading conditions. Thus, this paper aims to develop a novel method to use the measured displacement field to calculate the crack strain energy release rate and the mode I-III stress intensity factors. At the same time, the fundamental principles and methodologies associated with mixed-mode cracking analysis, stereo digital image correlation techniques, and using the Arcan fixture in experimental studies will be discussed For mixed mode fracture, including mode I, II, and III, stereo-DIC (or 3D DIC, i.e., using more than one camera) is a useful technique for tracking cracks and other discontinuities in materials, and also provides in- and out-of-plane surface displacement and deformation fields. By combining experimental and novel analytical approaches that calculated the in situ mixed-mode SIFs, we seek to show how the combination of Arcan and stereo-DIC provides insights into the behaviour of materials under mixed-mode loading, which can further improve our understanding of crack growth and fracture mechanisms.

2. Method

The study builds on the techniques established by Becker et al. [30], Molteno and Becker [7] and Koko et al. [39] to combine Arcan testing and digital image correlation to establish mixed-mode fracture properties from laboratory-scale samples. A comprehensive review of the extraction of SIFs from DIC computed displacement data can be found here [40]. Following these, we outline the details of our experimental methods below.

2.1. Arcan test fixture

Mechanical testing utilised the modified version of the Arcan fixture proposed by Yen et al. [41], which involved bolting a butterfly-shaped specimen between two symmetrical semi-circular steel discs. The specimen had trapezoidal cut-outs for fitting before bolting. Yen et al. [41] demonstrated that a homogeneous stress and strain field can be achieved with a central butterfly-shaped specimen, now known as the "butterfly specimen".

Polymethyl methacrylate (PMMA, also known as Perspex or Plexiglass) was used as a homogeneous and isotropic material, exhibiting near-linear elastic brittle fracture at room temperature [42]. Clear-cast PMMA CT specimens were laser cut from a 6 mm sheet to the butterfly geometry (Fig. 1). Sharp pre-cracks were induced from a 15 mm starter notch to a total length of approximately 20 mm, with crack tips located within a 2 mm² region at the specimen's centre. The samples were secured using six M6x1 bolts (three on each side, thus fully constraining the specimen). We determined the respective tensile properties using uniaxial tensile tests according to ASTM D638 as follows: Young's modulus, E=3GPa, and Poisson's ratio, v=0.36. Furthermore, the mode I fracture toughness value for PMMA was determined as $K_{Ic}=1.7$ MPa.m $^{0.5}$, averaged from three ASTM E1820 compact tension (CT) specimen tests with W=50mm and B=12mm.

We use a modified Arcan fixture that allows for testing for the three modes of failure; it consists of two rotating halves that can be adjusted in 15° increments in two rotation axes to facilitate the independent contribution of modes I and III (Fig. 1). By adjusting the loading points of the fixture, different crack loading configurations are possible,

¹ The subscript 1 denotes the predefined direction of crack propagation, i.e., J_1 assumes the crack advances only in x_1 in a locally defined coordinate system.

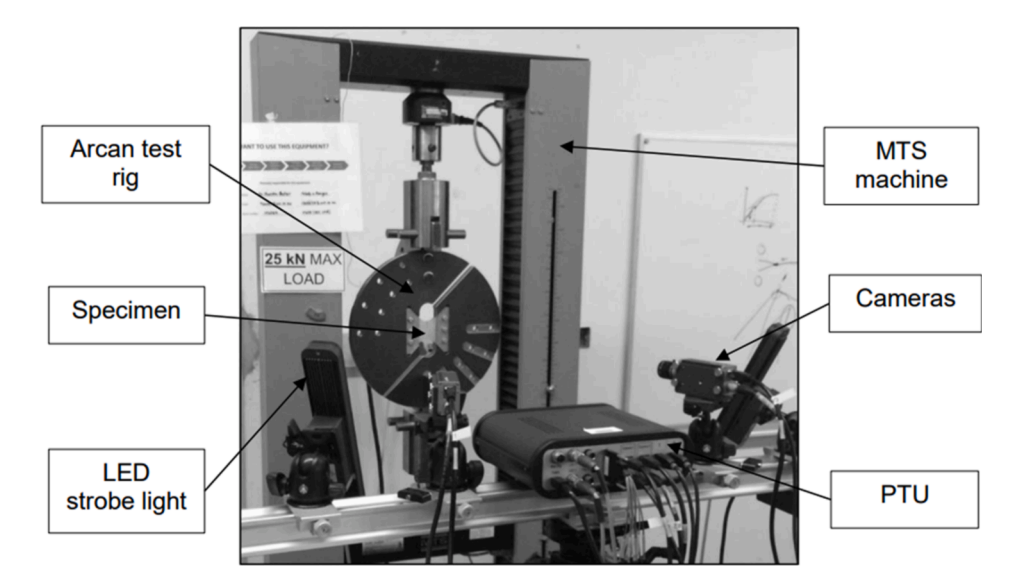


Fig. 1. The Arcan test fixture with the butterfly sample and digital image correlation system.

ranging from pure tensile (i.e., mode I loading) to pure in-plane shear (i. e., mode II loading) and an out-of-plane shear contribution (i.e., a mode III contribution).

In its neutral orientation, the fixture is loaded using the tensile test clevis to impose mode I loading (i.e., the crack plane is perpendicular to the loading axes). Mapping the clevis about the out-of-plane axis contributes to mode II loading, thereby maintaining the sample surface parallel to the loading axis. Rotation angles of 0, 30, 45 and 90 were considered. Contributions to mode III loading is achieved by rotating the clevis about the in-plane axis to tilt the sample relative to the loading axis. Rotation angles of 0, 30, and 45 were considered. The rig is prevented from lateral and rotational movement by constraining the fixture to the tensile machine using two pins required to induce mixed-mode loading.

The samples were tested in displacement control at a 5 mm/min rate.

2.2. Digital image correlation

A stereo-DIC system was employed to account for in- and out-of-plane surface deformation measurements to capture mode I-III loading. The system consisted of two Lavision TM (LaVision Gmbh) Imager E-lite 12-bit cameras equipped with 5-megapixel Sony ICX625 CCD sensors and two LaVision TM linear arrays of 12 white LEDs each that produce light with a radiometric power of 20 W. System-specific parameters are summarised in Table 1 in accordance with the iDICs guidelines [43]. The system was calibrated using a LaVision TM stereo-DIC calibration plate.

Table 1DIC system parameters.

Image resloution	2,058 by 2,456 pixel
Field of view	110 by 131 mm
Stand-off distance	550 mm
Image acquisition rate	$1~\mathrm{Hz^\dagger}$
Magnification factor	15 pixel/mm
Patterning technique	White base coat with black speckles via spray can
Pattern feature size (average)	6–10 pixels

† The experiments were performed under quasi-static loading conditions, where the crack growth is relatively slow, and sudden crack propagation events are less common. During these tests, the crack growth was stable and progressive, which allowed us to capture the crack tip displacement field with sufficient resolution using a 1 Hz acquisition rate. Furthermore, the focus of our study was on understanding the fracture process during mixed-mode loading rather than capturing ultra-fast crack propagation events associated with dynamic fracture.

The Arcan fixture was loaded using a Criterion Series 40 (MTS Systems cooperation) frame fitted with a 30 kN load cell. The cameras were aligned for each specific mixed-mode setup to ensure the crack tip is approximately located at the centre of each camera and to ensure a similar field of view between different mode configurations. The data were DIC-analysed using DaVis v.10.2 (LaVision GmbH). Relevant DIC process parameters are summarised in Table 2 in accordance with the iDICs guidelines [43].

Rigid body movement correction was done using the approach described in [44]. Rigid body movement refers to the combined translation and rotation of an object, without changing the shape or deformation of the object itself. The correction involved identifying the point with the absolute minimum displacement at the origin [34]. This provided a displacement noise floor of 2.9 μm .

2.3. Integral analysis

We employ a finite element method to extract SIFs using the J-integral from displacement data that was acquired using DIC. The J-integral quantifies the strain energy release rate for the crack propagation using the DIC local measurements without knowing the external boundary conditions. Compared to using the Williams' series least square fitting method, it is less sensitive to knowledge of the exact position of the crack tip [40].

To do this, we used the displacement information as boundary conditions within a finite element model of a crack. We use a MATLAB code that operates within the ABAQUS software to streamline this process. We ensure that our finite element (FE) model aligns with the DIC analysis results by adjusting the spacing of the FE mesh nodes to match the regular DIC grid, employing square elements. This alignment allows us to avoid interpolation when applying the DIC displacement field to the FE mesh. We then locally refine the FE mesh to introduce the crack in regions where the DIC displacement vectors are "censored" due to noise. Additionally, the mesh density near the crack tip was tripled to capture

Table 2 DIC process parameters.

Subset size	41 pixels (Guassian-weighted)
Step size	4 pixels
Subset shape function	Second order
Matching criterion	Zero-normalised sum of squared differences (ZNSSD)
Interpolant	Bicubic spline
Displacement noise floor	2.9 μm

steep displacement gradients and intense stress concentrations accurately. This finer mesh is crucial for resolving strain and displacement fields, which is essential for calculating SIFs. Previous studies showed that a threefold increase ensures convergence of the J-integral and accurate SIF extraction without excessive computational cost [45]. This refinement balances accuracy and computational efficiency.

To ensure accurate results, we increase the mesh density threefold at the crack's tip [24,46]. This is due to the steep displacement gradients, where a finer mesh is required to accurately resolve the strain and displacement fields, which are critical for calculating the SIFs [46 45].

Nodal displacements are imposed based on the measured displacement vectors. These local boundary conditions are applied throughout the model except in the "censored" region, which can deform freely based on surrounding conditions and material properties. We then assign a material law to the model; in our study, we use the ABAQUS FE software package and a linear elastic material law requiring E and V.

To ensure that the region of interest (ROI) was not compromised at inclined positions, a portion of the full field of view (representing approximately 35 by 35 mm) was used. This region was approximately 8 mm from the clamps and within 3 mm from the crack tip. This selection ensured even stress distributions throughout the specimen's thickness. Consequently, *J*-integral contours were chosen between 3 and 12 mm from the crack tip.

The entire displacement field was analysed using the mode decomposition technique. This technique divides the displacement field into three distinct components: a symmetric field (u^I), an in-plane antisymmetric field (u^{II}), and an out-of-plane antisymmetric field (u^{III}); the mode of interest is separated by a sum or difference operation on the reflected and non-reflected fields about the crack plane (Equation (1). The decomposed fields expand the measured field, creating a representation of symmetry that simultaneously satisfies the equilibrium equation and a presumed traction-free boundary condition along the crack faces.

$$u = u^{I} + u^{II} + u^{III} = \frac{1}{2} \left\{ \begin{array}{l} u_{x} + \overline{u}_{x} \\ u_{y} - \overline{u}_{y} \\ u_{z} + \overline{u}_{z} \end{array} \right\} + \frac{1}{2} \left\{ \begin{array}{l} u_{x} - \overline{u}_{x} \\ u_{y} + \overline{u}_{y} \\ 0 \end{array} \right\} + \frac{1}{2} \left\{ \begin{array}{l} 0 \\ 0 \\ u_{z} - \overline{u}_{z} \end{array} \right\}$$
(1)

or

$$u = u^{l} + u^{II} + u^{III} = \frac{1}{2} \left\{ \begin{array}{l} u_x + \overline{u}_x \\ u_y - \overline{u}_y \end{array} \right\} + \frac{1}{2} \left\{ \begin{array}{l} u_x - \overline{u}_x \\ u_y + \overline{u}_y \end{array} \right\} + \frac{1}{2} \left\{ \begin{array}{l} u_z + \overline{u}_z \\ u_z - \overline{u}_z \end{array} \right\}$$
(2)

The ABAQUS® v.6.14 finite element solver was utilised to evaluate the strain energy release rate $(J^{I,II,III})$ and corresponding stress intensity factors for each decomposed field. This was achieved by applying the nodal displacements of the u^I , u^{II} and u^{III} fields as boundary conditions in a simplified two-dimensional geometry, as described in Equation (2). The stress intensity factors K_I and K_{II} were obtained from the u^I and u^{II} fields, respectively, without the need for assuming $u_z + \overline{u}_z = 0$. The antisymmetric shear stress intensity factor K_{III} and is associated symmetric out-of-plane contribution to mode I $(K_I^{out \text{ of plane}}, \text{ i.e., } \frac{1}{2}(u_z + \overline{u}_z))$ was calculated from the u^{III} field using the mode decomposition algorithm [47]. Then, both the in and out-of-plane mode I were combined as shown in Equation (3).

$$K_{I} = K_{I}^{\text{in plane}} + K_{I}^{\text{out of plane}}$$
(3)

The calculations used a rectangular grid spacing with four nodes for each plane stress element (ABAQUS® CPS4). ABAQUS allows for the consideration of linear elastic material properties, and the implementation of equivalent domain integration (EDI) [48–50], rather than line integration, to evaluate the magnitude and sign of the three-dimensional stress intensity factors [51]. The EDI approach started at the tip of the crack. It propagated in the local direction of a virtual extension, with the linear spatial variation across nodes determined using a smooth function (q) that is set as unity at the tip and zero at the

outer domain. We define the q-vector normal to the crack front, aligning it with the linear segment of the crack path closest to the crack tip. The J-integral calculation is performed over multiple contours to ensure the results are independent of the chosen contour. This allows us to determine the potential release of elastic strain energy associated with crack propagation based on the measured displacement field.

It is important to note that the sign of in-plane shear (II) and out-of-plane shear (III) is irrelevant in this context, as it depends on the node arrangement at the tip and does not have any physical significance [52]. However, the sign of mode I is crucial as it characterises the presence of tensile or compressive conditions at the tip of the slip band. It should also be emphasised that the sign of the symmetrical out-of-plane contribution to mode I is not influenced by the sign of the mode III stress intensity factor.

The resulting values of the J integral and the SIF values were obtained as J^i and K_i from the u^i (where i designate the mode) displacement field as given in Equation (2). Furthermore, based on the work of Cottrell and Rice [53], it was established that for mixed-mode crack loading, the total strain energy release rate, J, is the sum of the energy release rates for each mode, as expressed in Equation (4).

$$J = J^I + J^{II} + J^{III} \tag{4}$$

3. Results and discussion

In the experimental setup, the specimen was securely affixed to the Arcan fixture (Fig. 2a) to allow for the application of multi-axial loads. The loading process was initiated at what is referred to as Stage 0 in Fig. 3a. This stage represents the initial displacement, which is the point at which the load begins to be applied to the specimen. It is a critical reference point in the testing procedure as it sets the baseline for subsequent measurements and observations.

In the initial loading stage (Stage I), the interval at which the images were captured versus the SIF plot, as depicted in Fig. 3, exhibits a linear elastic regime, forming the fracture zone ahead of the crack. As the load increases (Stage II), cracks extend toward the mode-specific crack front, influenced by loading conditions. In the concluding stages of loading (Stage III), the fracture becomes unstable, leading to rapid crack growth and sudden, catastrophic failure. The fracture path remains dependent on mixed-mode loading conditions.

After testing, images were analysed, and stress intensity factors (SIFs) were computed. For each imaging interval, the strain energy field around the crack tip was evaluated by calculating the mode-specific J-integral as the integration domain expanded from the crack tip. The mode-specific J-integral converged once the displacement singularity ahead of the crack was engulfed by the integration domain. Initial nonconvergence of the J-integral can be due to the breakdown of the elasticity assumption and elevated localised plasticity or poor discretisation of the strain data near the crack tip [54], but stable convergence was achieved as the domain expands. The characteristic mode-specific J-integral values were taken from the stable converged region (shaded area in Fig. 2b), with variance indicating convergence stability. The mode-specific J-integral values were then used to calculate the mode I-II-III stress intensity factors through the Young's modulus, shear modulus, and Poisson's ratio. In addition, the total *J*-integral is the sum of the mode-specific integrals (shown in read in Fig. 2b).

The values for linear gradient increment for Stage I in SIFs, stable SIFs values in Stage II, and linear gradient of Stage III are summarised in Table 3 for all loading conditions.

3.1. ModeI

The loading was set to induce a tensile (mode. I) loading. The initial stages (Stage I) show slower increases in K_I , K_{II} , K_{III} , and the J-integral, corresponding to crack initiation. Initially, K_I values were low, reflecting the early stages of crack initiation, where the crack begins to open under

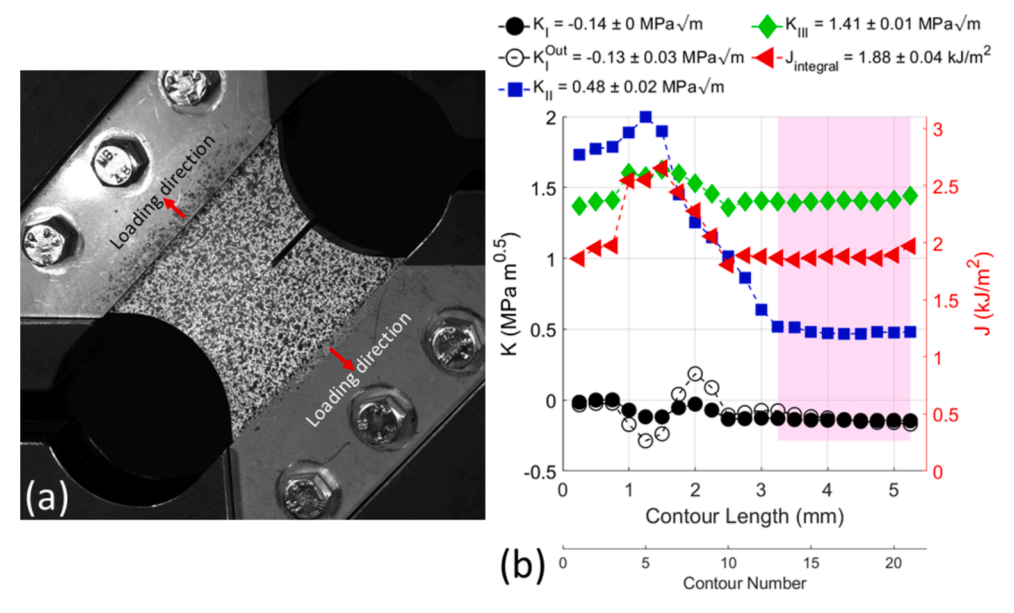


Fig. 2. (a) Imaging field of view for a butterfly sample loaded in mode I with 45° mode II and 45° mode III contributions at 183 intervals. (b) Example of calculated *J*-integral and decomposed stress intensity factors (SIFs) for the 32nd interval when the sample was loaded in mode II with 45° mode III. The integration contours start from the crack tip and expand in q-direction, parallel the crack, at 0.25 mm increments. The part of the contour shaded in pink was used to calculate the mean values presented in the legend.

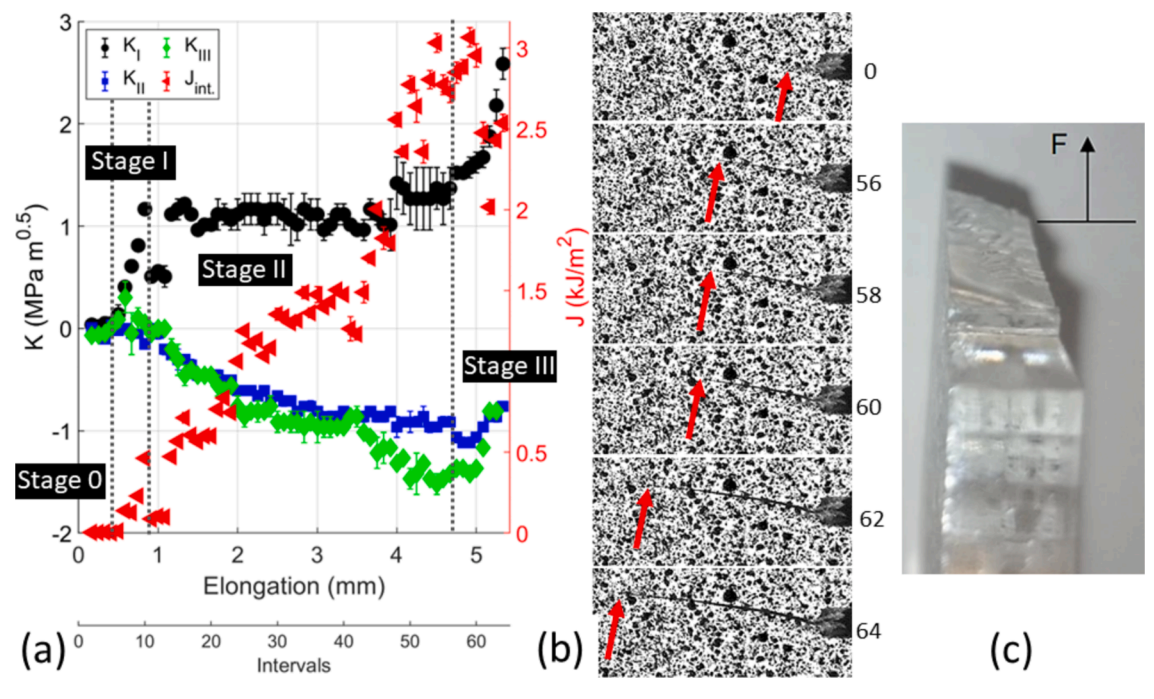


Fig. 3. (a) Applied pure mode I loading intervals of the crack while being in displacement control and calculated in and out of plane mode I—III stress intensity factors (SIFs). (b) Crack growth in Stage III of fracture numerated per interval. (c) The final fracture surface.

applied tensile stress. This phase is characterised by minimal material separation and the beginning of stress concentration at the crack tip. In this stage, the gradient for the crack being loaded was 3.04 \pm 0.03 MPa $m^{0.5}/mm$.

As K_I values increased up to the end of Stage I (Fig. 3a), which signified the transition from crack loading to propagating through the material. This stage is marked by a controlled, steady increase in crack length under increasing applied load. The stress intensity factor at this stage remains below the material's fracture toughness (K_{IC}). For this test, Stage I was defined by the stable K_I values. However, even though the test is supposed to be in pure mode I (great care was taken in

machining, setting up and aligning the fixture), computed SIFs from the measured displacement field reveal parasitic in and out-of-plane shear, resulting in mode II and III contributions. The non-zero K_{II} and K_{III} values, increasing as the test continued, can occur due to factors like fixture alignment, specimen geometry, or loading conditions. The variations in K_{II} and K_{III} across intervals might reflect complex interactions of different loading modes contributing to overall crack behaviour and growth, albeit secondary to the primary mode I loading scenario.

Overall, during Stage II, the crack experienced an average of 1.14 \pm 0.14 MPa m $^{0.5}$ mode I SIF, 0.69 \pm 0.23 MPa m $^{0.5}$ mode II SIF, and 0.85

 \pm 0.41 MPa m^{0.5} mode III SIF, with a total strain energy release rate of 1.38 \pm 0.78 kJ/m². The (negative) sign of the shear mode II and III SIFs depend on the chosen node arrangement at the crack tip and lack physical meaning [52].

A sharp increase in K_I indicates the material was approaching its fracture toughness, where the crack grew rapidly and uncontrollably, leading to the final fracture. This stage represents a critical point where the material can no longer withstand the applied stresses, culminating in catastrophic failure. The gradient for the crack loading in mode I in this stage was 3.91 ± 0.08 MPa m $^{0.5}$ /mm, accompanied by parasitic mode II of 0.85 ± 0.03 MPa m $^{0.5}$ /mm and mode III of 3.48 ± 0.14 MPa m $^{0.5}$ /mm. In addition, as shown in Fig. 3b, in the final stage of fracture (Stage III), the crack exhibited a gradual change in direction, explaining the ultimate deviation of the surface (Fig. 3c) from the fracture surface expected in pure mode I loading. In pure mode I, the crack front is semi-elliptical, and the crack surface is flat in homogeneous materials like PMMA, occurring perpendicular to the applied tensile stress [71], contradicting Fig. 2c and further substantiating the stereo-DIC observed parasitic shear.

The J-integral represents the energy release rate as the crack propagates and provides a measure of the crack driving force in the material. An increasing trend in the J-integral values through the intervals, mirroring the crack growth stages, from initiation through stable growth, until the rapid propagation just before failure. The J-integral's behaviour complements the observations made from K_I , K_{II} , and K_{III} , offering an energy-based perspective on the crack growth process. It provides a holistic view of how the material dissipates energy under applied stresses, which is particularly useful for materials with nonlinear elastic or plastic behaviour at the crack tip.

3.2. Mode I with 15° modeIII

The loading was configured to create a mix of tensile mode I and outof-plane shear mode III conditions. This was done by altering the loading points on the fixture by 15° . The mode III loading contributions were made possible by rotating the clevis around the in-plane axis and tilting the sample about the loading axis. The rig was kept stable and prevented from moving laterally or rotating by securing the fixture to the tensile machine using two pins. This was necessary for inducing mixed-mode loading.

Like the mode I loading, the crack displayed the three loading stages that are visible in Fig. 4a, where there is a progressive increase in K_I and K_{III} by a gradient of 0.75 \pm 0.01 MPa m^{0.5}/mm and 0.87 \pm 0.02 MPa m^{0.5}/mm, respectively, emphasising the primary role of tensile stresses (mode I) in initiating and driving the crack growth, and the additional tearing mode stresses at a 15° orientation, contributing to the cracking behaviour. This trend reaffirms the crack's extension under opening mode conditions, with a steady increase indicating the material's response to tensile loading. In addition, Fig. 4a shows that these out-of-plane shear stresses, while secondary to the primary mode I stresses, play a significant role in the material's overall fracture response.

As K_{II} and K_{III} values increased up to the end of Stage I (Fig. 4a), identified by the subsequent stabilising of the SIFs in Stage II as the loaded crack minimally but steadily propagates through the material. Furthermore, although the focus is not on mode II loading, the presence of K_{II} values and their variations across intervals suggest minor influences of shear stresses on the crack propagation. Overall, during Stage II, the crack experienced an average of 1.04 ± 0.08 MPa m^{0.5} mode I SIF, 1.10 ± 0.06 MPa m^{0.5} mode III SIF, and a minimal 0.11 ± 0.05 MPa m^{0.5} mode II SIF, with a total strain energy release rate of 1.47 ± 0.12 kJ/m². After stage II, the crack grew rapidly before the final fracture.

After 44 imaging intervals, a sudden 0.15 ± 0.04 MPa m^{0.5} increase in K_I and 0.12 ± 0.05 MPa m^{0.5} in K_{II} that lasted up to the 50 intervals. Upon closer inspection of the images and the displacement fields, we saw no visible changes indicating this change's source. Thus, we assumed it was due to an error in locating the crack tip, which can influence the strain energy release rate calculation by approximately 0.08 % per pixel [46]. Please see [64] and Appendix (5.C) for more detailed error analysis.

After Stage II, a sharp increase in K_I and K_{III} , indicating rapid crack growth with a steep gradient of mode I and III equal 1.14 ± 0.03 MPa m^{0.5}/mm and 0.72 ± 0.06 MPa m^{0.5}/mm, respectively. In addition, the fracture surface resulting from the mixed load in mode I and III can be complex and is characterised by a combination of features from both

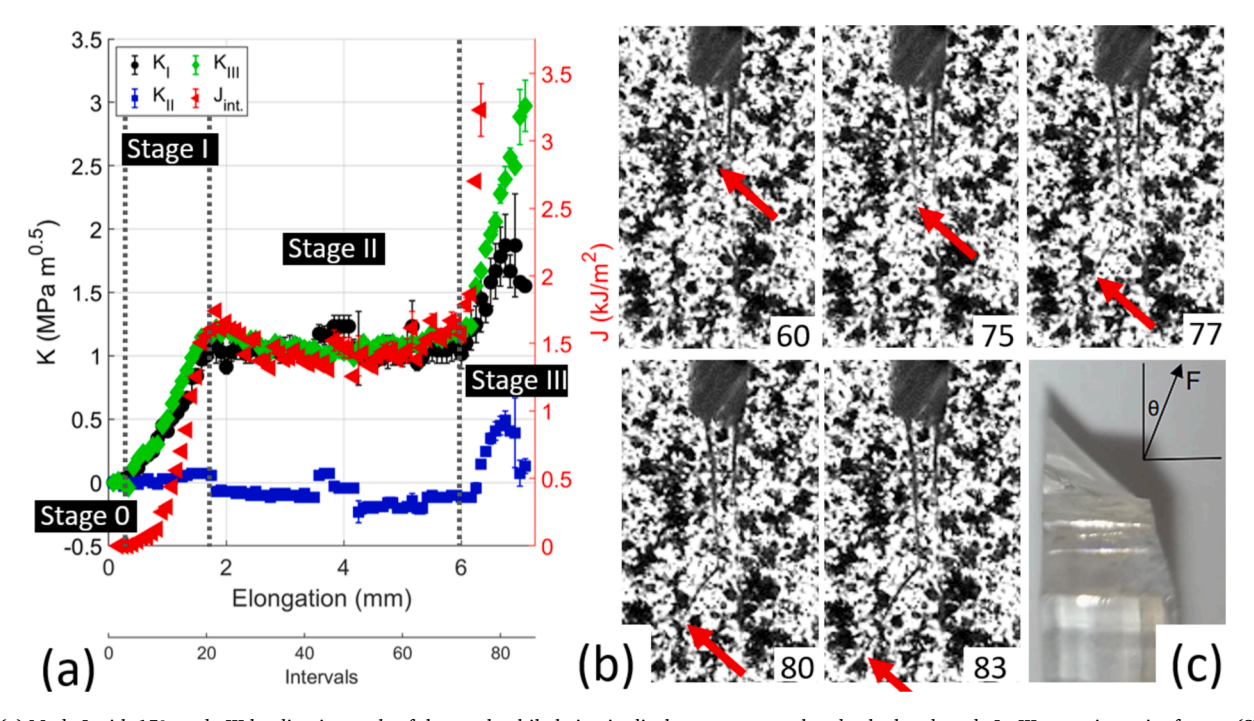


Fig. 4. (a) Mode I with 15° mode III loading intervals of the crack while being in displacement control and calculated mode I –III stress intensity factors (SIFs). (b) The crack angle is inferred from *J*-integral calculation. (a) Crack growing in Stage III. (b) Crack surfaces of specimens under mode I with 15° mode III.

loading modes. From the fracture propagation images (Fig. 4b), the direction of the crack was straight during initial growth. However, it started to change direction gradually as it reached stage III, resulting in the fracture surface (Fig. 3c), which was initially flat and then serrated at an angle corresponding to the crack direction.

Similar to the mode I, the *J*-integral's trend across intervals provides insight into the energy release rate and crack driving force, reflecting the cumulative effects of K_I , K_{II} , and K_{III} . The progressive increase in the *J*-integral, alongside changes in K_I and K_{III} highlights the material's energy absorption and dissipation behaviour as it responds to applied stresses. However, different from mode I, the *J*-integral matched K_I and K_{III} behaviour, due to the minimal mode II, which means that mode II was likely induced due to intrinsic material properties and behaviour under stress, rather than a problem in the fixture.

3.3. Mode I with 45° modeIII

The loading was adjusted to enhance the out-of-plane shear mode III conditions by modifying the fixture's loading points by 45°. Like the previous loading conditions, the crack experienced the three regimes of loading; however, there was a longer Stage I region of slow initial crack loading (Fig. 5a) with a K_{III} gradient of 0.59 \pm 0.01 MPa m^{0.5}/mm, followed by Stage II, and similar Stage III gradient of 0.57 \pm 0.00 MPa m^{0.5}/mm for mode III. During Stage II, the crack experienced an average of 1.45 \pm 0.03 MPa m^{0.5} mode II SIF, and minimal 0.17 \pm 0.03 MPa m^{0.5} mode I SIF and 0.09 \pm 0.03 MPa m^{0.5} mode II SIF, with a total strain energy release rate of 1.93 \pm 0.08 kJ/m².

Variations in K_I and K_{II} across intervals indicate the influence of tensile and in-plane shear stresses on the crack's initiation and propagation, with stress conditions at the crack tip being mainly due to out-of-plane shear stresses from tearing mode loading at a 45° angle. Overall, the trend observed in the J-integral values reflect the cumulative energy release rate associated with crack growth, and indicated, similar to the mode I with 15° mode III loading, that K_I and K_{II} are intrinsic and not due to the fixture. An increasing J-integral indicates the escalating availability of energy for crack propagation, informed by the contributions of K_I , K_{II} , and K_{III} .

After 36 imaging intervals (Fig. 5a) there was a sudden 0.06 ± 0.00 MPa m^{0.5} increase in K_I that lasted for 3 intervals. Upon closer inspection, no apparent changes were found in the image and displacement

field; the change was assumed to be due to an error in accurately locating the crack tip.

In addition, the fracture surface showed evidence of shearing in a direction parallel to the plane of the crack, and the fracture surface was inclined to the original plane of the crack (Fig. 5c) as mode III loading occurs when shear stress is applied to the crack faces in a direction perpendicular to the plane of the crack. Here, the crack faces slide past each other in this direction, forming a fracture surface that appears rough and jagged, with little or no opening of the crack faces. This fracture surface is typical for mode III loading [2].

3.4. ModeII

The loading was set to induce in-plane shear mode II conditions. Given the complexity of applying mode II conditions, additional mode I and III were observed by stereo-DIC. As for Stage I, the crack was loaded with a steep gradient of K_I that equalled 0.71 \pm 0.02 MPa m^{0.5}/mm and a K_{II} with a 0.15 \pm 0.00 MPa m^{0.5}/mm gradient. But K_{III} had a parabolic increment that dropped when the crack reached Stage II.

Across Stage II, which is defined by the stabilising of mode II values, the crack experienced an K_I of 1.26 ± 0.11 MPa m $^{0.5}$ and K_{II} of 0.43 ± 0.03 MPa m $^{0.5}$, and a fluctuating K_{III} of 0.83 ± 0.33 MPa m $^{0.5}$, with a total strain energy release rate of 1.33 ± 0.50 kJ/m 2 . Once the crack reached the unstable crack propagation region, K_I decreased whereas K_{II} and K_{III} increased, all with a similar gradient of -0.69 ± 0.01 MPa m $^{0.5}$ /mm, 0.64 ± 0.01 MPa m $^{0.5}$ /mm, and 0.61 ± 0.03 MPa m $^{0.5}$ /mm, respectively, before the crack rapidly ran across the entire sample. Similar to the previous tests, the J-integral's progression across intervals reflects the energy release rate and the overall crack driving force.

In general, a mode I contribution is to be expected as a pure mode II loading is not possible using an Arcan setup, due to the elastic deformation of the sample, resulting in some rotation and hence crack opening [55]. In addition, the mode III contribution can be the crack tip intrinsic to stabilise the crack propagation. However, because its contribution increased during the test, it is most likely due to misalignments in the setup, similar to what was observed for the mode I test.

A sudden change in the direction of the crack occurred as the crack abruptly changed in length and direction, leading to failure between two frames that were taken 1 s apart (Fig. 6b). The fracture surface shown in Fig. 6c resulted from sliding (mode II) and tearing (mode III). This

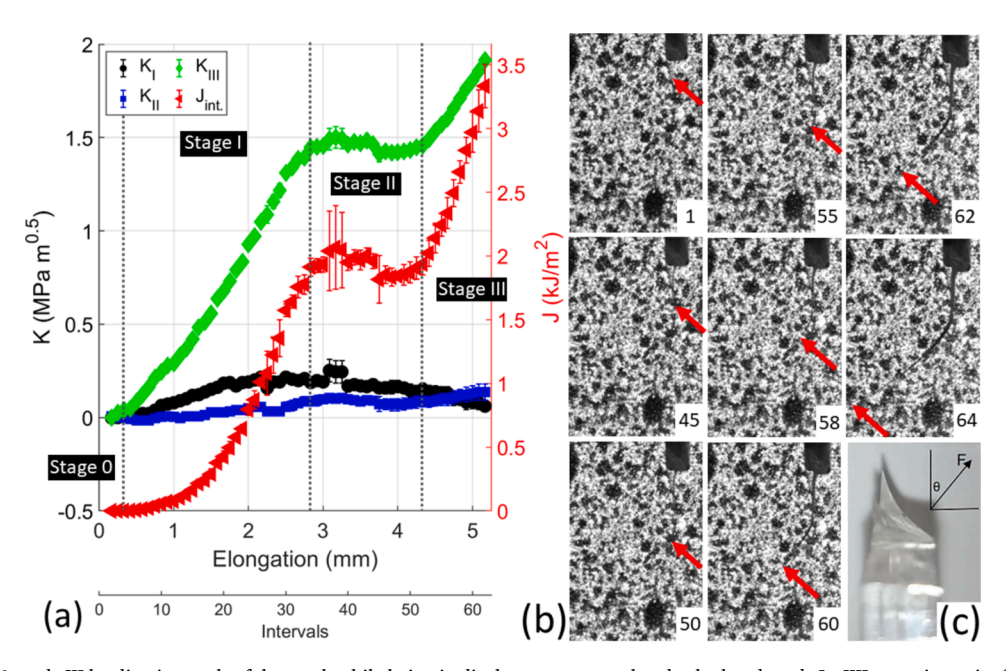


Fig. 5. Mode I with 45° mode III loading intervals of the crack while being in displacement control and calculated mode I –IIII stress intensity factors (SIFs). (b) Stage III crack growth under mode I with 45° mode III loading. (c) Specimen final surface.

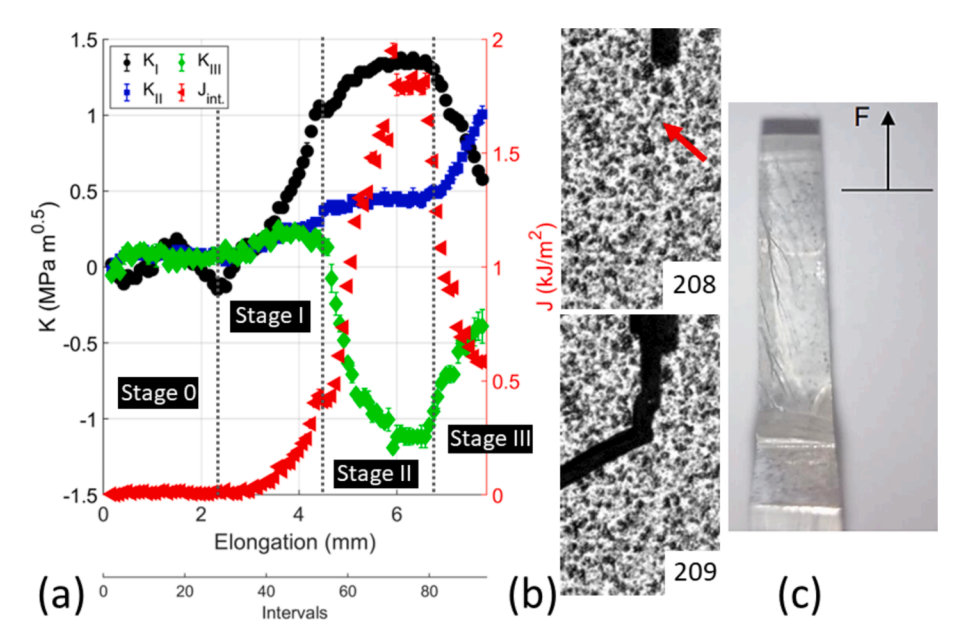


Fig. 6. (a) Pure mode II loading intervals of the crack while being in displacement control and calculated mode I – III stress intensity factors (SIFs). (b) Crack growth in the last two loading intervals in what was assumed to be a pure mode II loading conditions. (c) The specimen's final fracture surface.

caused the crack surfaces to slide relative to each other, resulting in shear stresses in the y-direction ahead of the crack.

3.5. Mode II with 15° modeIII

By adjusting the loading points of the fixture at 15° , the loading was set to induce a combination of mode II and III conditions at the crack tip. Stage I saw the in-plane shear stresses (sliding mode) K_{II} and out-of-plane shear stresses (tearing mode) K_{III} values increased by 0.48 \pm 0.01 MPa m^{0.5}/mm and 1.25 \pm 0.03 MPa m^{0.5}/mm, respectively

(Fig. 7a). However, like the mode I with 15° mode III setup, an unintended mode I contribution was uncovered using the stereo-DIC setup, suggesting that tensile stresses (opening mode) also influence the crack tip's stress state. Similar to mode I with 15° mode III loading, K_I seems to be intrinsic as it stabilised in Stage II.

During Stage II (Fig. 7a) the crack experienced an average of 1.41 \pm 0.12 MPa $m^{0.5}$ mode III SIF, 0.48 \pm 0.01 MPa $m^{0.5}$ mode II SIF, and minimal compressive -0.12 ± 0.03 MPa $m^{0.5}$ mode I SIF, with a total strain energy release rate of 1.89 \pm 0.25 J/m².

Following 25 imaging intervals (as shown in Fig. 7a), K_{II} and K_{III}

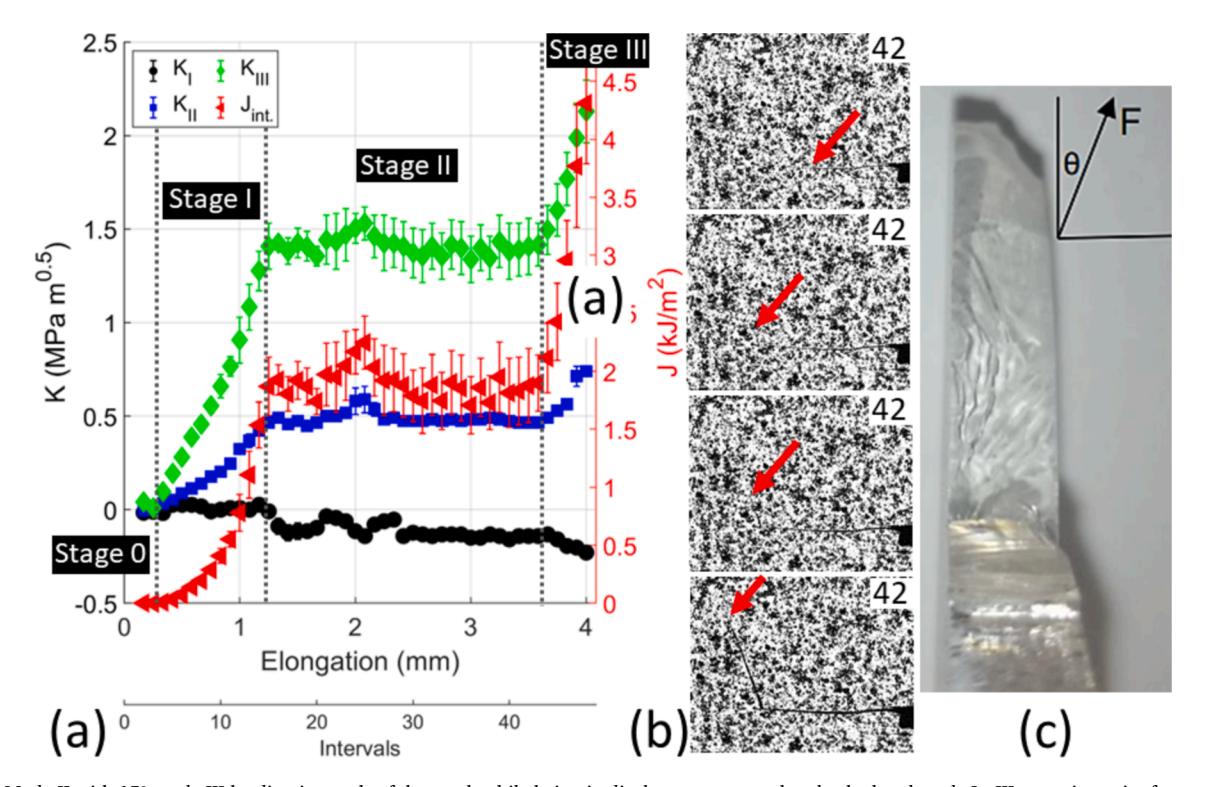


Fig. 7. (a) Mode II with 15° mode III loading intervals of the crack while being in displacement control and calculated mode I –III stress intensity factors (SIFs). (b) Stage III crack growth at final 42, 45, 47 and 49 intervals. (c) The crack surface of the specimen under mode II with 15° mode III.

exhibited a slow upward trend, while K_I showed a reduction throughout the three intervals. Despite a thorough examination revealing no noticeable alterations in the image and displacement field, it was inferred that the observed changes were likely attributable to inaccuracies in pinpointing the exact location of the crack tip.

Then, during Stage III, mode II and III increased linearly with a 0.32 $\pm~0.01$ MPa m $^{0.5}$ /mm and 1.9 $\pm~0.02$ MPa m $^{0.5}$ /mm gradients, respectively and a decrease in mode I by a $-0.17~\pm~0.03$ MPa m $^{0.5}$ /mm. In Stage III, the crack started to kink due to the slide and tearing of the crack surface (Fig. 7b) due to mode II and mode III loading and minimal compressive mode I. The final fracture surface (Fig. 7c) showed craze marks with an inclined and jagged fracture surface.

Overall, as seen in Fig. 7a, the trends in K_{II} and K_{III} stress intensity factors provide valuable insights into how the combined shear and tearing stresses drive crack propagation, with no significant mode I contribution. The simultaneous occurrence and variation of K_I , K_{II} , and K_{III} underline a complex stress environment at the crack tip, where sliding (mode II) and tearing (mode III) stresses are predominant but influenced by incidental opening stresses. This was accompanied by the increasing trend in the J-integral across intervals, reflecting the energy aspects of crack growth, highlighting the transition from crack initiation through stable growth to rapid propagation and eventual fracture under the combined effects of shear and tearing loading. In general, the crack behaviour is similar to the mode I with 15° mode III loading.

3.6. Mode II with 45° modeIII

The loading was adjusted to enhance the out-of-plane shear mode III conditions by adjusting the fixture's loading points by 45° angle. Like the previous loading conditions, the crack experienced the three regimes of loading (Fig. 5a); however, there was a longer Stage I region – similar to mode I with 15° mode III loading observations – as initial crack loading has a K_{III} gradient of 0.24 \pm 0.00 MPa m^{0.5}/mm, followed by Stage II, and Stage III gradient of 0.37 \pm 0.01 MPa m^{0.5}/mm for mode III.

During Stage II, the crack experienced an average of 1.48 ± 0.06 MPa m $^{0.5}$ mode III SIF, and minimal compressive -0.10 ± 0.01 MPa m $^{0.5}$ mode I SIF and 0.13 ± 0.02 MPa m $^{0.5}$ mode II SIF, with a total strain energy release rate of 2.00 ± 0.16 kJ/m 2 . In Stage II, after 115 imaging intervals, there was a sudden 0.13 ± 0.03 MPa m $^{0.5}$ decrease in K_{III} probably due to an error in identifying the crack tip.

Variations in K_I and K_{II} across intervals indicate the fluctuating, yet minimal, influence of tensile and in-plane shear stresses on the crack's initiation and propagation, with stress conditions at the crack tip mainly due to out-of-plane shear stresses from tearing mode loading at 45°. Overall, the trend observed in the J-integral values reflect the cumulative energy release rate associated with crack growth, and indicated, similar to the mode II with 15° mode III loading, that K_I and K_{II} are intrinsic and likely not due to a misalignment in the fixture. An increasing J-integral indicates the escalating availability of energy for crack propagation, informed by the contributions of K_I , K_{II} and K_{III} .

Fig. 8b indicates that the crack's kink is mainly due to the mode III tearing of the crack surface (see additional supplementary videos). As the test continued, the crack kept curving until the final fracture (Fig. 8c), where the fracture surface also showed craze marks with a curved fracture surface.

3.7. Mode I with 45° mode II and 45° modeIII

The loading encompassed a complex mixed-mode fracture scenario combining mode I-III at a 45° orientation to induce mode I-II-III. This setup is designed to investigate the interplay of opening, sliding, and tearing stresses on crack propagation, which is crucial for understanding material response under realistic loading conditions that often involve multiple stress modes.

Stage I saw a steep mode III gradient of 0.57 \pm 0.00 MPa m^{0.5}, K_{II} gradient of 0.21 \pm 0.00 MPa m^{0.5}, and K_{I} of 0.17 \pm 0.00 MPa m^{0.5}, matched with similar ascending order of 0.13 \pm 0.01 MPa m^{0.5}, 0.21 \pm 0.00 MPa m^{0.5}, and 0.62 \pm 0.00 MPa m^{0.5} gradients for mode I-II-III. During Stage II of the crack growth, the crack experienced an average of 0.44 \pm 0.02 MPa m^{0.5} mode I SIF, 0.50 \pm 0.04 MPa m^{0.5} mode II SIF, and 1.35 \pm 0.02 MPa m^{0.5} mode III SIF, with a total strain energy release rate of 1.81 \pm 0.16 J/m².

After 13 imaging intervals (Fig. 9a) there was a sudden increase in K_I by 0.02 ± 0.01 MPa m^{0.5}, K_{II} by 0.02 ± 0.02 MPa m^{0.5}, and K_{III} by 0.04 by 0.04 by 0.04 m^{0.5}, and 0.04 m^{0.5}. Also, after 43 imaging intervals, there was a sudden increase in 0.04 m^{0.5}, and 0.04 m^{0.5}, 0.04 m^{0.5}, 0.04 m^{0.5}, and 0.04 m^{0.5}, and 0.04 m^{0.5}. Upon closer inspection of the images and displacement data, the behaviour – like other instances – can be attributed to the uncertainties in defining the crack tip location.

There were no obvious signs of fixture-induced additional loading, and similar to the previous crack loading that involved mode II, the

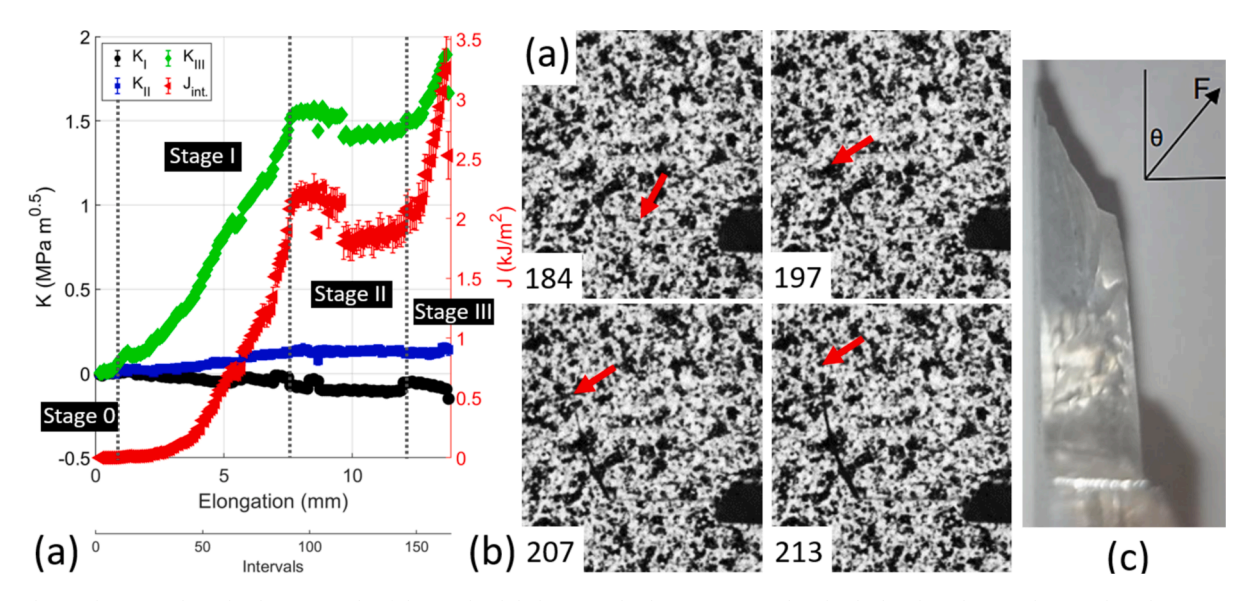


Fig. 8. Mode I with 45° mode III loading intervals of the crack while being in displacement control and calculated mode I, mode II, and mode III stress intensity factors (SIFs). (b) The crack angle is inferred from *J*-integral calculation. Crack (a) growth and (b) final fracture surface of specimens under mode II with 45° mode III.

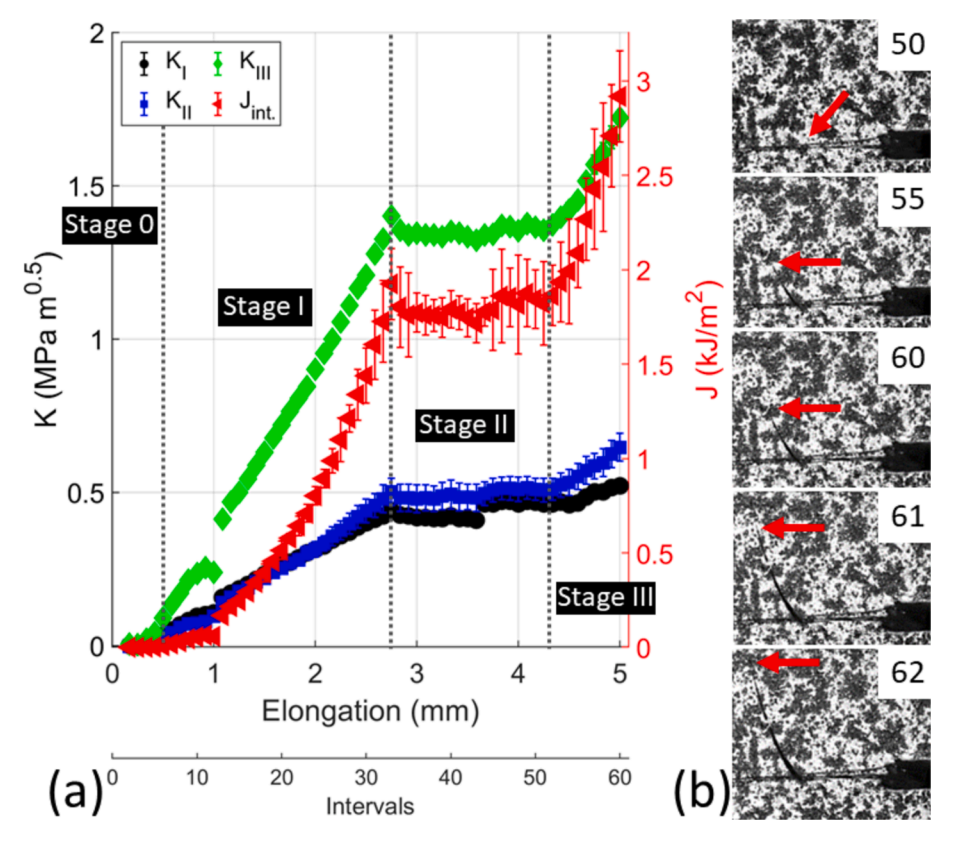


Fig. 9. Mode I with 45° mode II and 45° mode III loading intervals of the crack while being in displacement control and calculated mode I –III stress intensity factors (SIFs). (b) The crack angle is inferred from *J*-integral calculation. (c) Crack growth in Stage III.

crack kinked and continued to curve as it grew (Fig. 9b) but due to a combination of in- and out-of-plane shear. Unfortunately, we could not retrieve the sample for imaging after the test.

3.8. Effective stress intensity factor

To predict mixed-mode crack growth behaviour, several criteria have been previously developed, such as the Maximum Hoop Stress criterion [56], Maximum Circumferential Stress criterion [57], and Minimum Strain Energy Density (SED) criterion [58,59]. Considering that the current calculation of SIFs is based on the potential energy release rate, using the Maximum Potential Energy Release Rate (MPERR) criterion [60] was deemed most appropriate. The MPERR criterion analyses crack propagation by considering the maximum potential energy release during growth, extending Griffith's fracture theory. It asserts that a crack will grow in the direction where the maximum energy is released, aiding in determining critical conditions for crack growth under complex loading conditions.

The calculated SIFs measured during stable crack growth in Stage II were then normalised by the effective or equivalent SIF (K_{eff}), calculated from Equation (5). The normalisation of SIFs measured during stable crack growth using the K_{eff} is a crucial aspect in understanding mixed-mode fracture mechanics and allows for the representation of the combined effects of modes I (opening), II (sliding), and III (tearing) on crack propagation. This approach, proposed by Chang et al. [60], leverages a three-dimensional fracture surface analysis to account for these mixed-mode contributions, providing a comprehensive understanding of crack growth dynamics. An alternative formulation based on the Huber-Mises criterion is available but applicable only to mode I/II and mode I/III cracks [61,62]. However, the K_{eff} is suited for slow and stable fracture, limiting its calculation to Stage II data.

$$K_{eff} = \sqrt{K_I^2 + K_{II}^2 + K_{III}^2} \tag{5}$$

$$\psi = \tan^{-1}\left(K_{III}/\sqrt{K_I^2 + K_{II}^2}\right)$$
 (6)

The normalised data fits well with the 3D surface from Chang et al. [60] (Fig. 10a) with an average $\rm R^2$ of 0.91. The normalised data is clustering in regions corresponding to the specific setup of mode I, II and III contributions. Data from the experimental setting to induce a pure mode II (K_{II}) and mode II with 45° mode III exhibited spreading due to the changing interplay between SIFs driving fracture during Stage II. In addition, the mode ratio angle, given by Equation (6), provides a better visualisation of the conditions at the mixed-mode crack (Fig. 10c). The colour zones, derived from the 3D surface, indicate the dominant cracking direction, and data fit well in these zones.

Similar to Fig. 10c, the experimental data can be fitted to critical surface constructed for the MPERR but using a constant value rather than K_{eff} . This value, which provides the best fit for all the data, is assumed to equal the material fracture toughness (K_{IC}). The best fit was at 1.82 MPa m^{0.5} with an R² of 0.95, which agrees with the mode I fracture toughness determined using ASTM E1820. A video that parametric-sweep of different K_{IC} and its effect on the fitting is included as a supplementary video. Nonetheless, the value of R² is rather qualitative for non-linear fitting [63] and cannot be used to estimate the uncertainty in the fracture toughness. From analysing the residuals between the fitting and raw data, the average uncertainty was around \pm 0.32 MPa m^{0.5}.

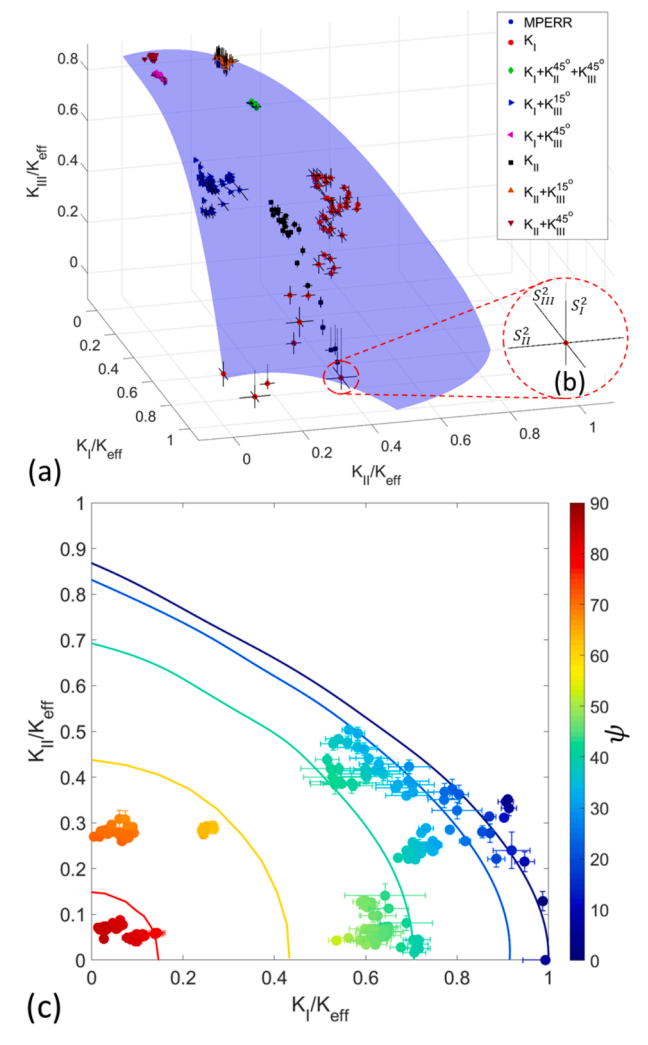


Fig. 10. (a) Fracture loci for the three-dimensional plot of the SIFs. (b) Solid black lines represent the uncertainty of measurement in mode I-III indicated as S_{I-III}^2 in the zoomed-in red circle. The vertically dotted black lines (see partially in at each point indicate the difference (parallel to the other axis) between the data and the surface. (c) Experimental data with the critical surface (equations (5) to (6) constructed at a constant value of K_{eff} for the mixed-mode maximum potential energy release rate (MPERR).

4. General discussion

4.1. Insights from the tests

Experimentally, we observed that the fracture in PMMA encompasses three stages: initiation (Stage I), propagation (Stage II), and fast unstable fracture (Stage III), each associated with distinct characteristics observable in the load–displacement curve, crack extension, and corresponding SIFs. In the initial loading stage (Stage I), the interval at which the images were captured versus the SIF plot, as depicted in Fig. 3, exhibits a linear elastic regime, forming the fracture zone ahead of the crack. At higher loads, crack propagation initiates near the specimen surface of the pre-crack front, especially pronounced in mixed-mode loading due to variations in the stress field around the crack.

As the load increases (Stage II), cracks extend toward the modespecific crack front, influenced by loading conditions. Studies on fracture propagation paths under mixed-mode loading in PMMA by Cooke & Pollard [64] reveal that the resulting crack geometry and its angle to the load line depend heavily on mixed-mode contributions. The craze zone on the fracture surface, formed during Stage II loading, reflects a process dependent on micro-deformation mechanisms occurring before or during slow crack propagation, independent of the loading angle [65]. The craze length was determined to be approximately 0.5 mm [66]. During this stage, relative stability in the elongation vs. SIF behaviour is observed, with the crack advancing steadily before the final fracture.

The crack's stable growth regime changes with the loading mode due to the inherent differences in the stress distribution and deformation mechanisms activated around the crack tip under different loading conditions. Each mode of loading—mode I (opening or tensile mode), mode II (sliding or shear mode), and mode III (tearing or out-of-plane shear mode)—introduces distinct stress fields and crack tip displacements, influencing the material's response and the crack propagation mechanisms. This complexity is critical for understanding material behaviour under realistic loading conditions, often involving multiple stress modes.

This is because in mode I, the crack faces are subjected to tensile stresses that open the crack. This mode typically results in a relatively straightforward crack propagation path, perpendicular to the direction of applied stress. The stable growth regime in mode I is characterised by a crack growth resistance that increases with a crack extension due to factors like material toughening mechanisms and crack path deflection.

Mode II introduces shear stresses that cause the crack faces to slide. As the material experiences shear-dominated deformation, the crack path can be more complex, often curving or branching. Stable crack growth in mode II may encounter different resistance mechanisms, such as microstructural barriers to shear displacement and frictional forces along the crack surfaces.

With mode III loading, the crack faces experience out-of-plane shear stresses, leading to tearing. The stable growth regime under mode III can be influenced by the material's resistance to tearing deformations, which may involve different microstructural and geometrical factors compared to modes I and II.

In the concluding stages of loading (Stage III), the fracture becomes unstable, leading to rapid crack growth and sudden, catastrophic failure. The fracture path remains dependent on mixed-mode loading conditions.

In general, the absence of pure mode loading in experimental setups, even when tests are designed to simulate pure modes, can be attributed to complex stress fields representing real-world scenarios where the stress fields around cracks are rarely uniform or singularly directional. Material anisotropy, heterogeneity, and geometric constraints can lead to complex stress distributions that introduce mixed-mode conditions. In addition, as a crack propagates, it may encounter microstructural features or inhomogeneities that alter its path. These deviations can change the local loading mode at the crack tip, introducing mixed-mode conditions even in tests designed for pure mode loading. The intrinsic material properties and behaviour under stress, such as plasticity and crack tip blunting, can affect the stress distribution and deformation around the crack tip, leading to the emergence of mixed-mode conditions.

However, these might not be issues related to the PMMA samples, although PMMA can undergo some plastic deformation as it exhibits elastic–plastic dominant deformation behaviour at the micron scale [78]. However, no significant plastic deformation region was observed in PMMA except for crazing marks, which were apparent in most tests and typically perceived as plastic deformation [67]. In future work, freezing to about –20 °C or UV aging [68] should be used to improve the brittleness of PMMA.

Also, achieving pure mode loading requires precise control over loading directions, magnitudes, and boundary conditions. Unavoidable deviations in the experimental setup, such as alignment errors or non-uniform load application, can introduce additional stress modes. Nonetheless, as shown in Table 3, the induced load was captured using stereo-DIC, revealing the unintended contribution to the stress state at the crack tip, which dictated the crack's growth path rate, loading rate, and overall fracture behaviour. This is because mixed-mode conditions, especially those combining mode II and mode III stresses present

Table 3
Summary of the stress intensity factors (SIFs) linear gradient for Stage I and III, and the average SIFs for Stage II.

		Stage I		
Test	$K_I(\text{MPa m}^{0.5}/\text{mm})$	$K_{II}(\text{MPa m}^{0.5}/\text{mm})$	K_{III} (MPa m ^{0.5} /mm)	
I	3.04 ± 0.03	_	_	
I/III 15°	0.75 ± 0.01	_	0.87 ± 0.02	
I/III 45°	_	_	0.59 ± 0.01	
II	0.71 ± 0.02	0.15 ± 0.00	_	
II/III 15°	=	0.48 ± 0.01	1.25 ± 0.03	
II/III 45°	=	_	0.24 ± 0.00	
I/II/III 45°	0.17 ± 0.00	0.21 ± 0.00	0.57 ± 0.00	
		Stage II		
Test	$K_I(\text{MPa m}^{0.5})$	$K_{II}(\text{MPa m}^{0.5})$	$K_{III}(\text{MPa m}^{0.5})$	Additional mode due to
I	1.14 ± 0.14	0.69 ± 0.23	0.85 ± 0.41	Fixture
I/III 15°	1.04 ± 0.08	0.11 ± 0.05	1.10 ± 0.06	Intrinsic
I/III 45°	0.09 ± 0.03	0.17 ± 0.03	1.45 ± 0.03	Intrinsic
II	1.26 ± 0.11	0.43 ± 0.03	0.83 ± 0.33	Fixture
II/III 15°	-0.12 ± 0.03	0.48 ± 0.01	1.41 ± 0.12	Intrinsic
II/III 45°	-0.10 ± 0.01	0.13 ± 0.02	1.48 ± 0.06	Intrinsic
I/II/III 45°	0.44 ± 0.02	0.50 ± 0.04	1.35 ± 0.02	None
		Stage III		
Test	$K_I(\text{MPa m}^{0.5}/\text{mm})$	$K_{II}(\text{MPa m}^{0.5}/\text{mm})$	K_{III} (MPa m ^{0.5} /mm)	
I	3.91 ± 0.08	0.85 ± 0.03	3.48 ± 0.14	
I/III 15°	1.14 ± 0.03	_	0.72 ± 0.06	
1/III 45°	_	_	0.57 ± 0.00	
II	-0.69 ± 0.01	0.64 ± 0.01	0.61 ± 0.03	
II/III 15°	-0.17 ± 0.03	0.32 ± 0.01	1.90 ± 0.02	
II/III 45°	_	_	0.37 ± 0.01	
I/II/III 45°	0.13 ± 0.01	0.21 ± 0.00	0.62 ± 0.00	

complex stress states that can significantly affect the material's fracture behaviour.

In addition, the change in crack stable growth regime with the mode of loading is supported by literature, indicating that different modes (I, II, and III) influence crack propagation directions and rates due to the varying stress fields and material response [1]. Mixed mode loading conditions further complicate crack growth behaviour, necessitating criteria for predicting crack growth directions under such conditions [69]. The complexities of achieving pure mode loading in experimental setups are highlighted by studies on crack arrest features and the influence of crack tip plasticity on determining and enhancing material resistance to crack growth.

The increasing trend in the J-integral across intervals encapsulates the energy aspects of the crack growth process, highlighting how the material's ability to absorb and release energy under applied stresses influences the progression towards fracture. The interplay between the energy release rate (J-integral) and the stress intensity factors (K_I , K_{II} , and K_{III}) provides a comprehensive view of the fracture process, from crack initiation through stable growth to the onset of rapid propagation and eventual failure, and offers invaluable insights into the mechanics of mixed-mode fractures and material resilience under combined loading conditions.

Fitting the experimental results to the MPERR criterion, a fracture toughness of 1.82 ± 0.32 MPa m0.5 was calculated. In general, the fracture toughness of PMMA typically ranges from 1.42 to 1.86 MPa m0.5 under quasi-static loading, while it can reach up to 2.5 to 4 MPa m $^{0.5}$. Moreover, our ASTM E1820 tests revealed a fracture toughness of 1.7 MPa m $^{0.5}$.

4.2. Mixed-mode testing

The existing literature presents various iterations of the Arcan fixture and specimen designs for mixed-mode testing. Notable variations include butterfly-shaped and square-shaped geometries, with notched and unnotched configurations reported. Circular fixtures are common, though exceptions exist [70]. When connecting the Arcan fixture to the load frame actuators, two main methods prevail: (1) a rotational

connection within the specimen plane and (2) a fixed connection limiting rotation at the fixture ends [70].

A freely rotating fixture is advantageous for alignment but poses challenges when imposing mixed-mode loading. Off-axis loading angles complicate the mixed-mode load, necessitating scrutiny of unwanted out-of-plane bending to prevent undesirable mode components in the SIF. This complexity is evident in pure mode I and II setups with mode III contributions. This is highlighted in the pure mode I and mode II setups presented in this study where contributions of mode III are present.

Precision in initiating the pre-crack is crucial to avoid errors in specimen and load orientations. Additionally, misalignment of the crack plane may introduce unwanted mode contributions, highlighting the need for careful examination. Moreover, minimising movement between components improves stability, reducing the chance of unwanted mode contributions. For example, the amount of "play" in the test rig (see the supplementary videos) during the experimental procedure could produce undesirable forces within the specimen. These seemingly negligible misalignments highlight the benefits of using an Arcan setup with stereo-DIC to capture actual conditions at the crack tip.

Modifications to the Arcan fixture aim to address non-uniformities and minimise mode III contributions for uniform stress states and pure plane strain conditions [71–75]. Although most modifications are validated analytically, one study validated a modified loading fixture using 3D finite element analysis and experiments on pre-cracked PMMA specimens [72]. However, asymmetry and unwanted mode III contributions in the modified Arcan fixture played a significant role in fracture results, particularly close to pure mode II loading angles, with up to a 42.65 % difference compared to a symmetrical fixture [76].

Previous attempts to calculate mixed-mode SIFs from the Arcan fixture relied on analytical solutions or simulation, often neglecting small mixed-mode load contributions — only some acknowledged that there might be a load skewness in their setup. In contrast, others recognised mixed-mode load contributions, using correction factors [77] or attributing inconsistencies between simulation and experiment crack trajectories to mode contributions [78]. Despite these variations, some observed good consistency between experimental results and finite element predictions [4,12,79], even without considering minor mode

contributions. These observations challenge previous conclusions that mixed-mode fracture tends to follow mode I crack, since mode I, observed from DIC data, is induced by in- and out-of-plane loading in tension and compression [80]. A study showed that as the load shifted from pure mode I to pure mode III, the fracture load increased while the corresponding fracture toughness value decreased [81].

The challenges extend beyond Arcan testing. A comparison between the International Organization for Standardization (ISO) and the American Society for Testing and Materials (ASTM) standards for measuring fracture toughness reveals significant experimental disparities of 58% [82] and 24% [80], with a theoretical inconsistency of 5% [83]. Notably, these figures do not account for additional uncertainties stemming from test system compliance and load misalignment.

Misalignment of the load introduces strain asymmetry on one side of the sample, intensifying during testing and diminishing the specimen's fracture toughness, especially in brittle materials [88–90]. This further underlines the complexities of fracture toughness measurements, emphasising the need for meticulous consideration of various factors influencing test outcomes and the inclusion of DIC in fracture testing.

4.3. Addition of stereo-DIC

As in the current work, local analyses utilising an Arcan fixture and stereo-DIC were shown to be valuable in scenarios where external conditions are uncertain. This approach offers alternatives to simulation and analytical solutions, acknowledging the absence of a simple boundary condition assumed in existing models. The reliability of results can be compromised when such conditions do not exist. Future methods improvements should address scalability and non-linearity, considering the incompleteness of the classic definition of the *J*-integral at the microscale, highlighted by large-scale yield phenomena [84].

During the experiment, the crack propagated at times faster than the image acquisition rate, emphasising the critical need for imaging during Stage II and III, especially during the sonic growth in mode II or III loading. Faster image acquisition would capture crucial details of crack behaviour and loading conditions that dominate crack propagation. Additionally, assumptions about the properties of homogeneous materials for heterogeneous materials need to be reconsidered, as variations in thickness permeability induced by the loading system affect the crack field in the sample [77].

Nonetheless, in the aforementioned literature, a planar medium is assumed, opening a different cane of warms when the assumption is invalid. For example, Vormwald et al. [85] investigated the use of stereo DIC to measure crack tip displacement fields on cylindrical surfaces under mixed-mode loading, addressing the variable mode-mixity encountered during fatigue crack growth. Their study highlighted the limitations of applying planar models to curved specimens, especially under mixed-mode conditions. Similarly, Camacho-Reyes et al. [86] developed a novel method for characterising non-planar crack tip fields using a differential geometry approach in combination with stereo DIC, allowing accurate measurement of crack tip displacements on curved surfaces such as thin-walled cylindrical specimens. Their approach extends traditional planar crack models to curved surfaces by incorporating 3D geometrical corrections. Lastly, Cao and Sipos [87] proposed a method for measuring the SIF of cracks in weakly curved brittle shells, demonstrating that traditional planar assumptions are insufficient for capturing the stress distribution in curved geometries. They applied a modified Williams expansion to curved shells and validated their approach through experimental tests on cylindrical and spherical shells. These studies collectively emphasise the complexity and necessity of considering non-planar geometries in fracture mechanics and provide methods that expand upon traditional planar approaches.

Hence, combining mixed-mode crack loading with threedimensional imaging and correlation, such as digital volume correlation (DVC), emerges as an insightful approach [25,88–91]. This integration can provide a comprehensive understanding of the strain distribution and crack development during shear testing. Such insights are essential for calibrating existing macro- and mesoscale models and testing methods, bridging gaps in our understanding of material behaviour under complex loading conditions.

4.4. Extraction of SIFs

The calculation of SIFs has been reported using various approaches, including field-fitting, integral methods, and more generalised crack opening displacement approaches. Additionally, cohesive zone models (CZMs) can be computed from displacement data, providing an alternative framework for analysing crack behaviour and propagation [40].

The choice of the J-integral is attractive since it does not necessitate precise knowledge of the crack tip and, in mixed-mode loading, only requires information about the crack plane. It eliminates the need for accurate DIC computed displacements near the crack tip, relying on data away from it. This study demonstrates the extraction of mixed-mode SIFs in complex mixed-mode testing, providing estimates for mode I, II, and III SIFs that align with experimental loading configurations. Furthermore, the obtained SIFs highlight unwanted mode contributions and facilitate the computation of the more general MPERR criterion. In addition, the new method shown here uses out-of-plane displacements, contrary to existing methods that use only in-plane displacements.

In this work, the crack direction remained constant, except in cases where shear was predominantly due to mode II. When controlled in mode I, the crack plane remained flat and did not curve, contrasting with the behaviour observed under shear control. Additionally, when the crack was under mode II loading, the rapid growth of the crack was sudden and less gradual compared to when it was controlled by mode I or mode III. These observations highlight the sensitivity of crack behaviour to different loading conditions, emphasising the need for nuanced analyses in mixed-mode scenarios, which can include using the *J*-vector analysis [92–94].

5. Conclusions

The study analyses mixed-mode fracture of Polymethyl methacrylate (PMMA) tested and monitored using an Arcan fixture coupled with stereo digital image correlation (DIC), which can measure the in- and out-of-plane surface displacement fields. The contribution of different loading modes was obtained by a novel method where the measured displacement field was decomposed into three distinct components: a symmetric field (u^{II}), an in-plane anti-symmetric field (u^{II}), and an out-of-plane antisymmetric field (u^{III}), which were used to calculate the mode-specific strain energy release rate (J-integral) and stress intensity factors (SIFs), including out-of-plane mode III without knowing the sample geometry or the nominal loading conditions.

In addition, the SIFs, measured during stable crack growth, were normalised by the effective SIF (K_{eff}) which fitted well against a fracture locus constructed using the Maximum Potential Energy Release Rate (MPERR) criterion. Using parametric sweeping, the fracture toughness (K_{IC}) found to equal 1.82 \pm 0.32 MPa m0.5, which agrees with values reported in the literature.

The methodology presented in this study, which combines Arcan fixture testing with stereo-DIC for mixed-mode fracture analysis, provides a comprehensive understanding of strain distribution and crack development and can be applied to a wide range of materials where inplane and out-of-plane loading conditions are relevant, including composites, metals, and polymers. However, the method is limited by the potential for parasitic loading modes inherent in the Arcan setup, as well as the need for careful alignment and calibration to ensure accurate displacement measurements and stress intensity factor extraction.

CRediT authorship contribution statement

Abdalrhaman Koko: Conceptualization, Software, Methodology, Visualization, Validation, Formal analysis, Writing – original draft. **Thorsten H. Becker:** Writing – original draft, Supervision, Resources, Formal analysis, Data curation.

Declaration of competing interest

The authors declare that they have no known competing financial interests or personal relationships that could have appeared to influence the work reported in this paper.

Acknowledgements

The authors thank Mr Erich Zahrt (University of Cape Town) for assisting with testing and data acquisition, and Dr Stefanos Giannis (National Physical Laboratory) for proofreading the article. The authors acknowledge the financial support from the University of Cape Town and the National Measurement System (NMS) programme of the UK government's Department for Science, Innovation and Technology (DSIT).

Appendix A. Supplementary material

Supplementary data to this article can be found online at https://doi.org/10.1016/j.tafmec.2024.104724.

Data availability

The Research data is available at https://doi.org/10.5281/zenodo.11098154.

References

- [2] H.A. Richard, B. Schramm, N.H. Schirmeisen, Cracks on Mixed Mode loading -Theories, experiments, simulations, Int. J. Fatigue 62 (2014) 93–103, https://doi. org/10.1016/j.jifatigue.2013.06.019.
- [3] Y. Wang, W. Wang, B. Zhang, C.Q. Li, A review on mixed mode fracture of metals, Eng. Fract. Mech. 235 (2020) 107126, https://doi.org/10.1016/j. engfracmech.2020.107126.
- [4] L. Gao, F. Ni, A. Braham, H. Luo, Mixed-Mode cracking behavior of cold recycled mixes with emulsion using Arcan configuration, Constr Build Mater 55 (2014) 415–422, https://doi.org/10.1016/J.CONBUILDMAT.2013.12.079.
- [5] I. Campione, T.M. Brugo, G. Minak, J.J. Tomić, N. Bogojević, S.Ć. Kostić, Investigation by digital image correlation of mixed mode I and II fracture behavior of metallic IASCB specimens with additive manufactured crack-like notch, Metals 10 (3) (2020) 400, https://doi.org/10.3390/MET10030400.
- [6] O. Demir, A.O. Ayhan, I.R.I.C. Sedat, H. Lekesiz, Evaluation of mixed mode-I/II criteria for fatigue crack propagation using experiments and modeling, Chinese Journal of Aeronautics 31 (2018) 1525–1534, https://doi.org/10.1016/j.cia.2018.05.009.
- [7] M.R. Molteno, T.H. Becker, Mode I-III Decomposition of the J-integral from DIC Displacement Data, Strain 51 (2015) 492–503, https://doi.org/10.1111/str.12166.
- [8] A.N. Danila, R. Steigmann, A. Savin, I. Blanari, P.D. Barsanescu, Arcan device employed in CFRP testing, in: 10th International Workshop NDT in Progress, 2019.
- [9] T. Laux, K.W. Gan, R.P. Tavares, C. Furtado, A. Arteiro, P.P. Camanho, et al., Modelling damage in multidirectional laminates subjected to multi-axial loading: Ply thickness effects and model assessment, Compos Struct 266 (2021) 113766, https://doi.org/10.1016/j.compstruct.2021.113766.
- [10] R. El-Hajjar, R. Haj-Ali, In-plane shear testing of thick-section pultruded FRP composites using a modified Arcan fixture, Compos B Eng 35 (2004) 421–428, https://doi.org/10.1016/j.compositesb.2003.12.004.
- [11] A. Esmaeili, E. Ghane, B. Mohammadi, On the use of digital image correlation for translaminar fracture of off-axis composite, Int J Fract 234 (2022) 195–212, https://doi.org/10.1007/S10704-022-00625-3/TABLES/4.
- [12] T. Chen, M. Ye, C. Yao, Z. Xiao, Fatigue behavior and digital image correlation monitoring of steel plates with mixed-mode edge cracks repaired with CFRP materials, Compos Struct 304 (2023) 116408, https://doi.org/10.1016/J. COMPSTRUCT.2022.116408.

- [13] T. Bonniot, V. Doquet, S.H. Mai, Mixed mode II and III fatigue crack growth in a rail steel, Int J Fatigue 115 (2018) 42–52, https://doi.org/10.1016/j. iifatigue.2018.01.010.
- [14] S.R. McNeill, W.H. Peters, M.A. Sutton, Estimation of stress intensity factor by digital image correlation, Eng Fract Mech 28 (1987) 101–112, https://doi.org/ 10.1016/0013-7944(87)90124-X.
- [15] S. Roux, F. Hild, Stress intensity factor measurements from digital image correlation: post-processing and integrated approaches, Int J Fract 140 (2006) 141–157, https://doi.org/10.1007/s10704-006-6631-2.
- [16] S. Yoneyama, Y. Morimoto, M. Takashi, Automatic Evaluation of Mixed-mode Stress Intensity Factors Utilizing Digital Image Correlation, Strain 42 (2006) 21–29, https://doi.org/10.1111/J.1475-1305.2006.00246.X.
- [17] S. Yoneyama, T. Ogawa, Y. Kobayashi, Evaluating mixed-mode stress intensity factors from full-field displacement fields obtained by optical methods, Eng Fract Mech 74 (2007) 1399–1412, https://doi.org/10.1016/J. ENGFRACMECH.2006.08.004.
- [18] G.J. Pataky, M.D. Sangid, H. Sehitoglu, R.F. Hamilton, H.J. Maier, P. Sofronis, Full field measurements of anisotropic stress intensity factor ranges in fatigue, Eng Fract Mech 94 (2012) 13–28, https://doi.org/10.1016/J. ENGFRACMECH.2012.06.002.
- [19] S. Rabbolini, G.J. Pataky, H. Sehitoglu, S. Beretta, Fatigue crack growth in Haynes 230 single crystals: an analysis with digital image correlation, Fatigue Fract Eng Mater Struct 38 (2015) 583–596, https://doi.org/10.1111/FFE.12261.
- [20] J. Carroll, C. Efstathiou, J. Lambros, H. Sehitoglu, B. Hauber, S. Spottswood, et al., Investigation of fatigue crack closure using multiscale image correlation experiments, Eng Fract Mech 76 (2009) 2384–2398, https://doi.org/10.1016/J. FNGFRACMECH 2009 08 002
- [21] M.Y. Tsai, J. Morton, New developments in the localized hybrid method of stress analysis, Exp Mech 31 (1991) 298–305, https://doi.org/10.1007/BF02325985.
- [22] S. Yoneyama, Smoothing Measured Displacements and Computing Strains Utilising Finite Element Method, Strain 47 (2011) 258–266, https://doi.org/10.1111/ i.1475-1305.2010.00765.x.
- [23] F. Caimmi, R. Calabrò, F. Briatico-Vangosa, C. Marano, M. Rink, J-Integral from Full Field Kinematic Data for Natural Rubber Compounds, Strain 51 (2015) 343–356, https://doi.org/10.1111/str.12145.
- [24] A. Koko, P. Earp, T. Wigger, J. Tong, T.J. Marrow, J-integral analysis: An EDXD and DIC comparative study for a fatigue crack, Int J Fatigue 134 (2020) 105474, https://doi.org/10.1016/j.ijfatigue.2020.105474.
- [25] A. Koko, S. Singh, S. Barhli, T. Connolley, N.T. Vo, T. Wigger, et al., 3-Dimensional analysis of fatigue crack fields and crack growth by in situ synchrotron X-ray tomography, Int J Fatigue 170 (2023) 107541, https://doi.org/10.1016/j. iifatigue.2023.107541.
- [26] Maugin GA. Configurational Forces. Boca Raton, Florida: Chapman and Hall/CRC; 2016. Doi: 10.1201/b10356.
- [27] G.C. Sih, P.C. Paris, F. Erdogan, Crack-Tip, Stress-Intensity Factors for Plane Extension and Plate Bending Problems, J Appl Mech 29 (1962) 306–312, https://doi.org/10.1115/1.3640546.
- [28] B. Roebuck, E. Bennett, L. Lay, R. Morrell, Measurement Good Practice Guide No 9: Palmqvist Toughness for Hard and Brittle Materials, Teddington (2008).
- [29] H. Bei, S. Shim, M.K. Miller, G.M. Pharr, E.P. George, Effects of focused ion beam milling on the nanomechanical behavior of a molybdenum-alloy single crystal, Appl Phys Lett 91 (2007) 111915, https://doi.org/10.1063/1.2784948.
- [30] T.H. Becker, M. Mostafavi, R.B. Tait, T.J. Marrow, An approach to calculate the J-integral by digital image correlation displacement field measurement, Fatigue Fract Eng Mater Struct 35 (2012) 971–984, https://doi.org/10.1111/j.1460-2695.2012.01685.x.
- [31] E. Breitbarth, T. Strohmann, M. Besel, S. Reh, Determination of Stress Intensity Factors and J integral based on Digital Image Correlation, Frattura Ed Integrità Strutturale 13 (2019) 12–25, https://doi.org/10.3221/IGF-ESIS.49.02.
- [32] S.M. Barhli, L. Saucedo-Mora, C. Simpson, T. Becker, M. Mostafavi, P.J. Withers, et al., Obtaining the J-integral by diffraction-based crack-field strain mapping, Procedia Structural Integrity 2 (2016) 2519–2526, https://doi.org/10.1016/j.prostr.2016.06.315.
- [33] A. Koko, E. Elmukashfi, K. Dragnevski, A.J. Wilkinson, T.J. Marrow, J-integral analysis of the elastic strain fields of ferrite deformation twins using electron backscatter diffraction, Acta Mater 218 (2021) 117203, https://doi.org/10.1016/j. actamat.2021.117203.
- [34] A. Koko, E. Elmukashfi, T.H. Becker, P.S. Karamched, A.J. Wilkinson, T.J. Marrow, In situ characterisation of the strain fields of intragranular slip bands in ferrite by high-resolution electron backscatter diffraction, Acta Mater 239 (2022) 118284, https://doi.org/10.1016/j.actamat.2022.118284.
- [35] M. Stern, E.B. Becker, R.S. Dunham, A contour integral computation of mixed-mode stress intensity factors, Int J Fract 12 (1976) 359–368, https://doi.org/10.1007/BF00032831.
- [36] H. Ishikawa, A finite element analysis of stress intensity factors for combined tensile and shear loading by only a virtual crack extension, Int J Fract 16 (1980) R243–R246, https://doi.org/10.1007/BF00016590.
- [37] A.F. Cinar, S.M. Barhli, D. Hollis, M. Flansbjer, R.A. Tomlinson, T.J. Marrow, et al., An autonomous surface discontinuity detection and quantification method by digital image correlation and phase congruency, Opt Lasers Eng 96 (2017) 94–106, https://doi.org/10.1016/J.OPTLASENG.2017.04.010.
- [38] J. Poissant, F. Barthelat, A Novel, "Subset Splitting" Procedure for Digital Image Correlation on Discontinuous Displacement Fields, Exp Mech 50 (2010) 353–364, https://doi.org/10.1007/s11340-009-9220-2.

- [39] A. Koko, T.H. Becker, E. Elmukashfi, N.M. Pugno, A.J. Wilkinson, T.J. Marrow, HR-EBSD analysis of in situ stable crack growth at the micron scale, J Mech Phys Solids 172 (2023) 105173, https://doi.org/10.1016/j.jmps.2022.105173.
- [40] T.H. Becker, Extracting fracture properties from digital image and volume correlation displacement data: A review, Strain (2023), https://doi.org/10.1111/ str.12469.
- [41] S.-C. Yen, J.N. Craddock, K.T. Teh, Evaluation of a modified Arcan fixture for the in-plane shear test of materials, Exp Tech 12 (1988) 22–25, https://doi.org/ 10.1111/J.1747-1567.1988.TB02169.X/METRICS.
- [42] L. Banks-Sills, M. Arcan, Mode II fracture toughness testing with application to PMMA, in: Application of Fracture Mechanics to Materials and Structures: Proceedings of the International Conference on Application of Fracture Mechanics to Materials and Structures, held at the Hotel Kolpinghaus, Freiburg, FRG, June 20–24, 1983, pp. 337–344, https://doi.org/10.1007/978-94-009-6146-3_18.
- [43] R. Bigger, B. Blaysat, C. Boo, M. Grewer, J. Hu, A. Jones, et al., A Good Practices Guide for Digital Image Correlation, International Digital Image Correlation Society (2018), https://doi.org/10.32720/idics/gpg.ed1.
- [44] M. Mostafavi, D.M. Collins, B. Cai, R. Bradley, R.C. Atwood, C. Reinhard, et al., Yield behavior beneath hardness indentations in ductile metals, measured by threedimensional computed X-ray tomography and digital volume correlation, Acta Mater 82 (2015) 468–482, https://doi.org/10.1016/j.actamat.2014.08.046.
- [45] T.H. Becker, M. Mostafavi, R.B. Tait, T.J. Marrow, An approach to calculate the J-integral by digital image correlation displacement field measurement, Fatigue Fract Eng Mater Struct 35 (2012) 971–984, https://doi.org/10.1111/j.1460-2695.2012.01685.x.
- [46] S.M. Barhli, M. Mostafavi, A.F. Cinar, D. Hollis, T.J. Marrow, J-Integral Calculation by Finite Element Processing of Measured Full-Field Surface Displacements, Exp Mech 57 (2017) 997–1009, https://doi.org/10.1007/s11340-017-0275-1.
- [47] A. Koko, DIC2CAE: Calculating the stress intensity factors (KI-III) from 2D and stereo displacement fields, ArXiv (2024), https://doi.org/10.48550/ arXiv.2409.08285.
- [48] D.M. Parks, The virtual crack extension method for nonlinear material behavior, Comput Methods Appl Mech Eng 12 (1977) 353–364, https://doi.org/10.1016/ 0045-7825(77)90023-8
- [49] C.F. Shih, B. Moran, T. Nakamura, Energy release rate along a three-dimensional crack front in a thermally stressed body, Int J Fract 30 (1986) 79–102, https://doi. org/10.1007/BF00034019.
- [50] F.Z. Li, C.F. Shih, A. Needleman, A comparison of methods for calculating energy release rates, Eng Fract Mech 21 (1985) 405–421, https://doi.org/10.1016/0013-7944(85)90029-3.
- [51] S. Courtin, C. Gardin, G. Bézine, B.H. Hamouda, H., Advantages of the J-integral approach for calculating stress intensity factors when using the commercial finite element software ABAQUS, Eng Fract Mech 72 (2005) 2174–2185, https://doi.org/ 10.1016/j.engfracmech.2005.02.003.
- [52] Systèmes® D. ABAQUS. ABAQUS v66 2009. https://classes.engineering.wustl.edu/ 2009/spring/mase5513/abaqus/docs/v6.6/index.html.
- [53] B. Cotterell, J.R. Rice, Slightly curved or kinked cracks, Int J Fract 16 (1980) 155–169, https://doi.org/10.1007/BF00012619.
- [54] J.D. Eshelby, The force on an elastic singularity, Philosophical Transactions of the Royal Society of London Series A, Mathematical and Physical Sciences 244 (1951) 87–112. https://doi.org/10.1098/rsta.1951.0016.
- [55] L.Z. Jin, C.Y. Zhou, C.Y. Yu, Q. Pei, L. Chang, X.H. He, Crack initiation characteristics of brittle materials with I-II mixed mode crack under uniaxial compression, Fatigue Fract Eng Mater Struct 45 (2022) 3067–3085, https://doi. org/10.1111/EFF.13787
- [56] C.A. Mixed-Mode, C. Propagation, Solid Mechanics and Its Applications 237 (2021) 179–236, https://doi.org/10.1007/978-94-024-2026-5_5/COVER.
- [57] F. Erdogan, G.C. Sih, On the Crack Extension in Plates Under Plane Loading and Transverse Shear, Journal of Basic Engineering 85 (1963) 519–525, https://doi. org/10.1115/1.3656897.
- [58] G.C. Sih, E.P. Chen, S.L. Huang, E.J. Mcquillen, Material Characterization on the Fracture of Filament-Reinforced Composites, Journal of Composite Materials 9 (1975) 167–186, https://doi.org/10.1177/002199837500900207.
- [59] G.C. Sih, Some basic problems in fracture mechanics and new concepts, Eng Fract Mech 5 (1973) 365–377, https://doi.org/10.1016/0013-7944(73)90027-1.
- [60] J. Chang, J. Xu, Y. Mutoh, A general mixed-mode brittle fracture criterion for cracked materials, Eng Fract Mech 73 (2006) 1249–1263, https://doi.org/ 10.1016/J.ENGERACMECH.2005.12.011.
- [61] D. Rozumek, Z. Marciniak, G. Lesiuk, J.A. Correia, A.M.P. de Jesus, Experimental and numerical investigation of mixed mode I + II and I + III fatigue crack growth in S355J0 steel, Int J Fatigue 113 (2018) 160–170, https://doi.org/10.1016/j. iifatigue.2018.04.005.
- [62] M. Duda, D. Rozumek, G. Lesiuk, M. Smolnicki, B. Babiarczuk, J. Warycha, Fatigue crack growth under mixed-mode I + II and I + III in heat treated 42CrMo4 steel, Int J Fract 234 (2022) 235–248, https://doi.org/10.1007/s10704-021-00585-0.
- [63] A.-N. Spiess, N. Neumeyer, An evaluation of R2 as an inadequate measure for nonlinear models in pharmacological and biochemical research: a Monte Carlo approach, BMC Pharmacol 10 (2010) 6, https://doi.org/10.1186/1471-2210-10-6.
- [64] M.L. Cooke, D.D. Pollard, Fracture propagation paths under mixed mode loading within rectangular blocks of polymethyl methacrylate, J Geophys Res Solid Earth 101 (1996) 3387–3400, https://doi.org/10.1029/95JB02507.
- [65] R. Lach, W. Grellmann, Mixed Mode Fracture Mechanics Behaviour of PMMA, Macromol Symp 373 (2017) 1600108, https://doi.org/10.1002/ MASY.201600108.

- [66] Chao Y-J, Zhang X. Constraint Effect in Brittle Fracture. Fatigue and Fracture Mechanics: 27th Volume, ASTM International100 Barr Harbor Drive, PO Box C700, West Conshohocken, PA 19428-2959; 1997, p. 41–60. Doi: 10.1520/STP16227S.
- [67] Y. Yan, Y. Sun, J. Su, B. Li, P. Zhou, Crazing Initiation and Growth in Polymethyl Methacrylate under Effects of Alcohol and Stress, Polymers (basel) 15 (2023) 1375, https://doi.org/10.3390/polym15061375.
- [68] S. Redjala, N. Aït Hocine, R. Ferhoum, M. Gratton, N. Poirot, S. Azem, UV Aging Effects on Polycarbonate Properties, Journal of Failure Analysis and Prevention 20 (2020) 1907–1916, https://doi.org/10.1007/S11668-020-01002-9.
- [69] R. Baptista, V. Infante, Fatigue crack propagation direction under different loading conditions using MTS and MSS criteria, Procedia Structural Integrity 37 (2022) 57–64, https://doi.org/10.1016/j.prostr.2022.01.059.
- [70] J.M. Greer, S.E. Galyon Dorman, M.J. Hammond, Some comments on the Arcan mixed-mode (I/II) test specimen, Eng Fract Mech 78 (2011) 2088–2094, https:// doi.org/10.1016/j.engfracmech.2011.03.017.
- [71] S.M.J. Razavi, F. Berto, A new fixture for fracture tests under mixed mode I/II/III loading, Fatigue Fract Eng Mater Struct 42 (2019) 1874–1888, https://doi.org/10.1111/ffe.13033.
- [72] M.R. Ayatollahi, B. Saboori, A new fixture for fracture tests under mixed mode I/III loading, European Journal of Mechanics, A/solids 51 (2015) 67–76, https://doi.org/10.1016/j.euromechsol.2014.09.012.
- [73] I. Ud Din, P. Hao, S. Panier, K.A.A. Khan, M. Aamir, G. Franz, et al., Design of a New Arcan Fixture for In-plane Pure Shear and Combined Normal/Shear Stress Characterization of Fiber Reinforced Polymer Composites, Exp Tech 44 (2020) 231–240, https://doi.org/10.1007/s40799-019-00353-9.
- [74] J.Y. Cognard, L. Sohier, P. Davies, A modified Arcan test to analyze the behavior of composites and their assemblies under out-of-plane loadings, Compos Part A Appl Sci Manuf 42 (2011) 111–121, https://doi.org/10.1016/j. compositesa.2010.10.012.
- [75] Czabaj MW, Audd C, Davidson BD, Ratcliffe JG. Development of a modified edge crack torsion test for mode III fracture toughness of laminated composites. ICF 2017 - 14th International Conference on Fracture 2017;2:704–5.
- [76] A.E. Oskui, N. Choupani, M. Shameli, 3D Characterization of Mixed-Mode Fracture Toughness of Materials Using a New Loading Device, Latin American Journal of Solids and Structures 13 (2016) 1464–1482, https://doi.org/10.1590/1679-78252779.
- [77] J. Xavier, M. Oliveira, J. Morais, T. Pinto, Measurement of the shear properties of clear wood by the Arcan test, Holzforschung 63 (2009) 217–225, https://doi.org/ 10.1515/HF.2009.034.
- [78] Galyon SE, Arunachalam SR, Greer J, Hammond M, Fawaz SA. Three Diminsional Crack Growth Prediction. In: Bos MJ, editor. ICAF 2009, Bridging the Gap between Theory and Operational Practice, Dordrecht: Springer Netherlands; 2009, p. 1035–68. Doi: 10.1007/978-90-481-2746-7 57.
- [79] S. Sajith, K.S.R.K. Murthy, P.S. Robi, Experimental and numerical investigation of mixed mode fatigue crack growth models in aluminum 6061–T6, Int J Fatigue 130 (2020) 105285, https://doi.org/10.1016/j.ijfatigue.2019.105285.
- [80] F. Ding, T. Zhao, Y. Jiang, A study of fatigue crack growth with changing loading direction, Eng Fract Mech 74 (2007) 2014–2029, https://doi.org/10.1016/j. engfracmech.2006.10.013.
- [81] M.R.M. Aliha, A. Bahmani, Rock Fracture Toughness Study Under Mixed Mode I/III Loading, Rock Mech Rock Eng 50 (2017) 1739–1751, https://doi.org/10.1007/ S00603-017-1201-7.
- [82] X. Li, Z. Ding, C. Liu, S. Bao, Z. Gao, Evaluation and comparison of fracture toughness for metallic materials in different conditions by ASTM and ISO standards, International Journal of Pressure Vessels and Piping 187 (2020) 104189, https://doi.org/10.1016/J.IJPVP.2020.104189.
- [83] S. Zhang, S. Zhou, M. Li, B. Fu, Calculation and comparison on fracture toughness of specific reliability between ASTM and ISO standards, Mater Res Express 7 (2020) 026529, https://doi.org/10.1088/2053-1591/AB6C21.
- [84] D. Wilson, Z. Zheng, F.P.E. Dunne, A microstructure-sensitive driving force for crack growth, J Mech Phys Solids 121 (2018) 147–174, https://doi.org/10.1016/j. jmps.2018.07.005.
- [85] M. Vormwald, Y. Hos, J.L.F. Freire, G.L.G. Gonzáles, J.G. Díaz, Crack tip displacement fields measured by digital image correlation for evaluating variable mode-mixity during fatigue crack growth, Int J Fatigue 115 (2018) 53–66, https://doi.org/10.1016/J.IJFATIGUE.2018.04.030.
- [86] A. Camacho-Reyes, J.M. Vasco-Olmo, M.N. James, F.A. Diaz, Characterization of non-planar crack tip displacement fields using a differential geometry approach in combination with 3D digital image correlation, Fatigue Fract Eng Mater Struct 45 (2022) 1521–1536, https://doi.org/10.1111/FFE.13686.
- [87] S. Cao, A.A. Sipos, About Measuring the Stress Intensity Factor of Cracks in Curved, Brittle Shells. Frattura Ed Integrità Strutturale 18 (2024) 1–17, https://doi.org/ 10.3221/IGF-ESIS.69.01.
- [88] Marrow J, Scotson D, Jin X, Chen H, Chen Y, Koko A, et al. Small-Specimen Testing, with Image-Based Analysis, for Crack Propagation Resistance in Polygranular Nuclear Graphite. Graphite Testing for Nuclear Applications: The Validity and Extension of Test Methods for Material Exposed to Operating Reactor Environments, ASTM International100 Barr Harbor Drive, PO Box C700, West Conshohocken, PA 19428-2959; 2022, p. 1–17. Doi: 10.1520/STP163920210051.
- [89] X. Zhang, Y. Deng, P. Yan, C. Zhang, B. Pan, 3D analysis of crack propagation in nuclear graphite using DVC coupled with finite element analysis, Eng Fract Mech 309 (2024) 110415, https://doi.org/10.1016/J.ENGFRACMECH.2024.110415.
- [90] H. Liu, F. Hild, Quantifying 3D crack propagation in nodular graphite cast iron using advanced digital volume correlation and X-ray computed tomography, Eng Fract Mech 296 (2024) 109824, https://doi.org/10.1016/J. ENGFRACMECH.2023.109824.

- [91] H. Chen, J. Shen, D. Scotson, X. Jin, H. Wu, T.J. Marrow, Fracture toughness evaluation of a nuclear graphite with non-linear elastic properties by 3D imaging and inverse finite element analysis, Eng Fract Mech 293 (2023) 109719, https://doi.org/10.1016/J.ENGFRACMECH.2023.109719.
- [92] L. Ma, T.J. Lu, A.M. Korsunsky, Vector j-integral analysis of crack interaction with pre-existing singularities, J. Appl. Mech., Trans. ASME 73 (2006) 876–883, https://doi.org/10.1115/1.2165243.
- [93] L. Ma, A.M. Korsunsky, On the use of vector J-integral in crack growth criteria for brittle solids, Int. J. Fract. 133 (2005) 39–46, https://doi.org/10.1007/s10704-005-0631-5
- [94] J. Scheel, A. Schlosser, A. Ricoeur, The J-integral for mixed-mode loaded cracks with cohesive zones, Int. J. Fract. 227 (2021) 79–94, https://doi.org/10.1007/ s10704-020-00496-6.